UPPSALA
UNIVERSITET

UPTEC F 17019
Examensarbete 30 hp
Juni 2017

Polycapillary X-Ray Optics for Liquid-Metal-Jet X-Ray Tubes

Engineering Physics, Applied Physics.
Excillum AB, Kista, Sweden.

Malcolm Lindqvist

UPPSALA
UNIVERSITET

Teknisk- naturvetenskaplig fakultet
UTH-enheten

Besöksadress:
Ångströmlaboratoriet
Lägerhyddsvägen 1
Hus 4, Plan 0

Postadress:
Box 536
751 21 Uppsala

Telefon:
018 – 471 30 03

Telefax:
018 – 471 30 00

Hemsida:
http://www.teknat.uu.se/student

Abstract

Polycapillary X-Ray Optics for Liquid-Metal-Jet X-Ray Tubes

Malcolm Lindqvist

Investigating and mapping fundamental processes in nature is a driving force for breakthroughs in research and technology. Doing so, requires knowledge of the smallest scales of the world. One way of performing measurements on these scales is through intense x-ray sources, which have improved greatly over the last decades. By combing these sources with state of the art optics, even higher flux densities can be reached, allowing for faster measurements and ground-breaking discoveries.

This study aims to explore the performance of polycapillary optics, when aligned to one of the most intense x-ray micro sources in the world, the liquid-metal-jet D2+. Knife edge scans were performed together with a photon-counting medipix x-ray camera to quantify focus properties such as, flux, flux density, transmission, gain and beam width. Measurements were conducted with a 20 μm source spot that was compared to a simulated 200 μm source spot, both at 260 W electron beam power. The data from vertical and horizontal scans were combined to reconstruct the 2D functionality of the polycapillary optic.

The flux density were almost four times higher with the 20 μm spot compared to the simulated 200 μm spot. This result correlated with the condition for total external reflection and the local divergence. The conclusion is that the small source spot of the liquid-metal-jet source improves the efficiency of the polycapillary optic.

The efficiency could still be improved, if the deviation in the pointing accuracy could be minimized. Furthermore, the combination of liquid-metal-jet x-ray source and the polycapillary optic, achieved extremely high flux densities, around: 2.4e13 $\frac{\text{photons}}{\text{s}\times\text{mm}^2}$. This was specially compared to an x-ray source used for confocal micro XRF, where the flux was almost nine times higher with the liquid-metal-jet x-ray source. This allows for faster measurements within confocal micro XRF and other techniques demanding very high flux densities, but with low demands on beam divergence and spectral purity.

Handledare: Ulf Lundström
Ämnesgranskare: Björgvin Hjörvarsson
Examinator: Tomas Nyberg
ISSN: 1401-5757, UPTEC F 17019

Sammanfattning

Att undersöka och kartlägga naturens fundamentala mekanismer är grundläggande för genombrott inom forskning och teknik. För att åstadkomma detta behövs information på de allra minsta skalor, vilket kan erhållas med en intensiv röntgenstråle. Genom att kombinera röntgenstrålen med toppmodern optik kan ännu högre flödestäthet uppnås. Detta möjliggör snabbare mätningar och därav ännu bättre möjligheter till banbrytande upptäckter.

Detta projekt ämnar att utforska prestandan som kan uppnås genom att kombinera den mest intensiva röntgenkällan i världen, liquid-metal-jet D2+, med toppmodern polykapilläroptik. Detta gjordes genom att konstruera en knivskannuppställning som användes tillsammans med en medipixkamera. En programvara skapades för att kontrollera knivbladet och medipixkameran, där programmet gav visuell återkoppling under mätningar. Programvaran extraherade datan från medipixkameran och sparade datan i en logisk struktur.

Därefter designades algoritmer för att kvantifiera parametrar i fokus så som flöde, flödestäthet, transmission, strålens bredd samt det pixel-visa beteendet för polykapilläroptiken. Mätningarna utfördes med en 20 μm källa som sedan jämfördes mot en större simulerad 200 μm källa. Knivskannmätningar i vertikalt och horisontellt led kombinerades för att åstadkomma den 2D prestandan av polykapilläroptiken.

Generellt sätt erhölls en signifikant förbättring: uppemot fyra gånger högre flödestäthet gentemot simuleringen. Detta korrelerade med relationen för den kritiska vinkeln och den lokala divergensen. Slutsatsen är att polykapilläroptiken fungerar bättre mot en mindre källa och att det kan potentiellt bli ännu bättre om kapillärernas pekningsnoggrannhet förbättras.

Kombinationen med liquid-metal-jet källan och polykapilläroptiken genererade extremt hög flödestäthet, runt: 2.4e13 $\frac{\text{fotoner}}{\text{s}\times\text{mm}^2}$. Mätningarna med samma polykapiläroptik jämfördes mot ytterligare en källa som används inom konfokalmikro XRF. Resultaten visade på uppemot nio gånger högre flöde med liquid-metal-jet kombinationen.

Acknowledgements

Foremost I would like to gratitude my family for the love an support throughout my studies and decisions in life. Without you I would not be where I am today. I will forever be thankful, you are truly the best.
I also want to thank Ulf Lundström for being the best supervisor that one could ask for. Your support and guidance through this thesis has been a great inspiration. I specifically appreciated your clear explanations together with endless positivity and encouragement.
I would also like to thank the CEO of Excillum, Björn Hansson, for the opportunity to work with your team and for believing in me. I really appreciated your great positivity and leadership and for letting me feel as part of the team. Furthermore, to all the employees at Excillum, thanks for your warm welcome and for making this a great environment to work in.
Last but not least, I would like to thank Björgvin Hjörvarsson for invaluable tips and recommendations and for your positive response.

Contents

Chapter 1

Introduction

The discovery of x-rays for medical imaging by W. C. Röntgen in 1895 led to a new era in science [1]. Since then, the technique of using x-rays to penetrate matter has revolutionized life science and technology [2]. Today the market continuously demands embedded systems that can generate brighter x-ray beams, where brightness is the flux per unit solid angle, where flux is the amount of photons per second. This allows for faster measurements with countless possibilities, especially for applications within x-ray diffraction, small angle x-ray scattering (SAXS) and x-ray fluorescence (XRF).

Currently, the best way to provide a beam with high brightness, requires a large impractical facility such as a synchrotron, with high costs of production and operation. However, there are sources that are less demanding to build and operate, but with lower brightness. These types of sources have previously been using an electron beam to impact on a solid rotating anode for x-ray generation. Over the years, substantial improvements have been made to the rotating anode and today there is marginal room for improvement.

In the last decade, a new concept has been developed, utilizing a liquid-metal-jet anode as target, instead of the solid rotating anode. This started at the Biomedical and X-ray Physics group at KTH, which later was commercialized by Excillum AB [3]. Since the anode is already molten it is possible to increase the electron beam power per unit area on the anode. This yields a source that delivers significantly higher brightness compared to any other micro focus x-ray source on the market, while still having room for improvement [4]. Furthermore, research has shown that tweaking the output of the beam can increase performance significantly.

This thesis investigates how state of the art x-ray optics, namely polycapillary optics, can improve the performance of the beam when aligned to a micro focus x-ray source. Previously this has been executed for larger x-ray spots [5], but small spots could potentially be even better, opening a new market for micro focus x-ray sources. Optimal performance is met when the x-ray source and the polycapillary optic are matched both in terms of design and alignment. Automated evaluation

and alignment schemes will be implemented using a medipix photon-counting camera in combination with a knife edge scan. This is done together with Excillum's x-ray source and the result could potentially be a door opener for customers within x-ray diffraction, SAXS and XRF.

Chapter 2

X-Ray Interaction with Matter

X-rays are electromagnetic waves with shorter wavelengths than visible light. Smaller wavelengths carries more energy per photon, which affect the interaction processes within a specific material. This chapter serves to provide a brief overview of the different interaction processes, appearing for the energy levels of interest. The energies of interest are the ones generated from the liquid-metal-jet, which currently can achieve energies in the upper boundary of soft x-rays to roughly the end of hard x-rays, see Fig. 2.1. Furthermore, principles for how x-rays can be focused via optics (reflection) will be given when using a liquid-metal-jet and also the processes that appears within the detectors designed for this energy span.

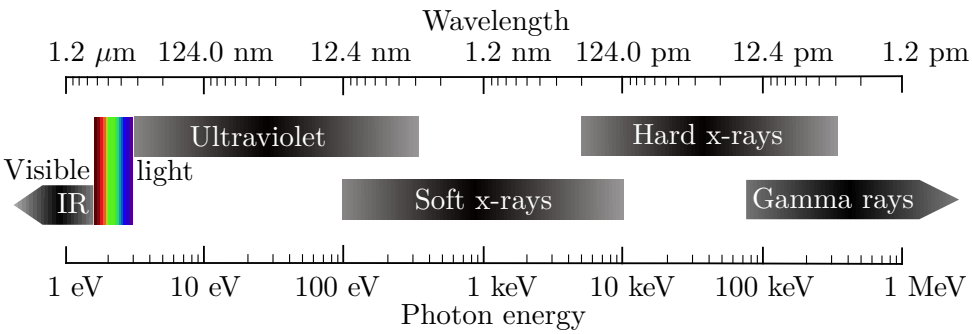

Figure 2.1: The electromagnetic spectrum from infrared (IR) to gamma rays.

2.1 Attenuation of X-Rays

When x-rays penetrate matter, the intensity is lost through absorption and scattering. It is these processes that are, utilized within medical computed tomography (CT), making medical imaging possible. In order to construct an image, the incoming penetrating x-rays need to have the right amount of energy. If too low

the entire electromagnetic (e-m) wave would be absorbed, with no radiation left to be measured at the detector. However, with enough energy the e-m wave is attenuated, though still measurable, thus making it possible to determine internal structures causing the attenuation. The attenuation of the incoming x-rays can be related to Beer-Lambert's law (law of attenuation) [6]

$$I(x) = I_0 \mathrm{e}^{-\mu x}, \tag{2.1}$$

where x is the distance that the x-ray travelled within a certain material, I_0 is the initial incoming intensity and μ is the attenuation coefficient for a specific material given monoenergetic radiation (radiation of same energy). The attenuation coefficient is found by measuring the penetration length, l, i.e. how deep an e-m wave can travel for a specific energy and material, $l = \frac{1}{\mu}$. The underlying reason for this attenuation within the energy scope of this context, is due to the following interactions: photoelectric effect (photoelectric absorption), incoherent (Compton) and coherent (Rayleigh) scattering. These are further described in subsection 2.1.1, 2.1.2 [2].

2.1.1 Photoelectric Effect

Photoelectric absorption, or the photoelectric effect appears when the incident x-ray photon is fully absorbed within the atom. As a result, all the energy of the incident x-ray photon is transferred to an electron, releasing it from the atomic core, see Fig. 2.2. This interaction dominates for hard x-rays of lower energies, and electrons are usually released from the inner shells of the atom. This happens when the energy of the incoming x-ray photon is larger than the binding energy of the electron and the surplus of energy is transferred as kinetic energy to the electron [7]. The excited atom is de-excited by two alternative processes, x-ray fluorescence or Auger emission. X-ray fluorescence occurs when one electron from a higher shell fills the vacancy, causing an x-ray to be emitted that is characteristic for the atom. The second process, Auger emission, causes a second electron to be ejected from the atom. This occurs when one electron from a higher shell fills the vacancy and the energy generated in the transition is larger than the binding energy of the bound electron.

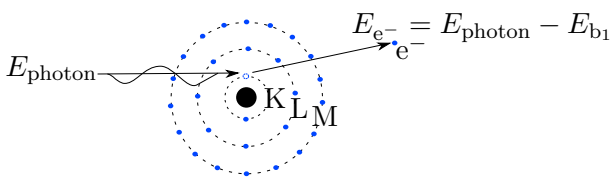

Figure 2.2: An incident photon with energy E_{photon}, ejects an electron from the inner shell K, with binding energy E_{b_1}. The rest of the energy is transferred to the electron, E_{e^-}, thus in total showing net effect of the photoelectric effect.

2.1.2 Incoherent and Coherent Scattering

Incoherent scattering, or Compton scattering, is a process where an incoming photon interacts with an electron. During the process the photon changes its direction and transfer some of its energy to the scattered electron, resulting in the net-effect of an inelastic process, see Fig. 2.3. The photon is scattered in a direction related to the amount of energy that is transferred to the electron [6]. For the energy range considered within this context, Compton scattering shows very little dependence on the energy of the incoming photon and atomic number. Photon counting detectors must handle the loss of the prior incoming photon since the secondary photon still can be measured within the detector.

Unlike incoherent scattering, coherent scattering is elastic and referred to as Rayleigh scattering for energies lower than electron binding energies. The process occurs when a strongly bound electron interacts with the electric field of an incoming x-ray photon. The elastic process implies that the electron moves just enough to conserve momentum at impact [8]. During the interaction the electron starts to oscillate with the same frequency as the incoming photon. The oscillating electron will then function in the same way as an antenna, thus emitting dipole radiation with the same frequency as the incoming x-ray photon see Fig. 2.3. Coherent scattering is stronger for lower x-ray energies and higher atomic numbers [2]. Other interesting properties such as Rayleigh scattering, explaining the blue color of the sky is well described in e.g. [9].

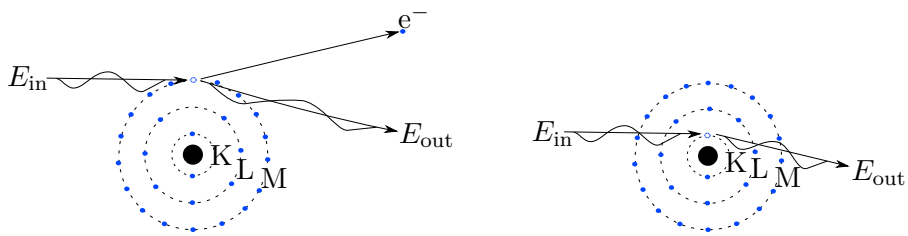

(a) Incoherent scattering (b) Coherent scattering

Figure 2.3: (a) In Incoherent (Compton) scattering the incident photon, E_{in}, interacts with a loosely bound electron and ionises the atom. (b) In coherent (Rayleigh) scattering the incident photon, E_{in}, interacts with electrons in an elastic manner, hence no energy loss of the outgoing photon ($E_{in} = E_{out}$).

2.1.3 Refractive Index

In order to understand the functioning of optical elements, it is important to know the fundamental properties of the refractive index. A relatively simple model is to treat the scattering electrons of the refracting atoms as oscillators. This model is not perfect, but as long as the frequency of the x-ray photon is larger than the corresponding electron resonance frequency, the model works well i.e. for $w_{\text{photon}} \gg w_{\text{electron}}$. The frequency of each atomic electron depends on its displacement within the atomic "shells". From the photoelectric effect in section, 2.1.1, each shell has specific resonance frequency w_{es} (or absorption frequency, where s denotes the orbital shell), meaning the model works well for energies above absorption edges. Treating each scattering electron as an oscillator gives the following equation of motion

$$\boldsymbol{F}_{\text{tot}} = \boldsymbol{F}_{\text{external}} - \boldsymbol{F}_{\text{damping}} - \boldsymbol{F}_{\text{restoring}}, \tag{2.2}$$

where the resulting force on the system of motion can be described via an external force responsible for the oscillation, a damping force resulting from the fact that an accelerating charge particle emits radiation, hence loss of energy and last a restoring force resulting from treating the atomic electrons as oscillators. By treating the incoming x-ray photon responsible for this oscillation as a plane wave and then solving the system for this force yields

$$m_{\text{e}}\frac{d\boldsymbol{x}^2}{dt^2} + m_{\text{e}}\gamma\frac{d\boldsymbol{x}}{dt} + m_{\text{e}}w_{\text{e}}^2\boldsymbol{x} = q\boldsymbol{E}(\boldsymbol{r},t) = q\boldsymbol{E}_{\text{incident}}\text{e}^{-i(w_{\text{photon}}t - \boldsymbol{k}\cdot\boldsymbol{r})}, \tag{2.3}$$

where m_{e} is the electron mas, γ is the damping factor, resulting from the energy loss during the acceleration of the charged electron, q is the electron charge, $E(\boldsymbol{r},t)$ the electric field amplitude of the incident plane wave with respect to vector position $\boldsymbol{r}$ and time t [10], $\boldsymbol{k}$ is the wave vector in the direction of the wave and the magnitude of wave vector $k = |\boldsymbol{k}|$ is the wave number k, where the wave number k is the number of wavelengths per unit distance $k = \frac{2\pi}{\lambda}$. Solving this inhomogeneous differential equation for the displacement $\boldsymbol{x}(t)$ and using the fact that the oscillation leads to a polarization, the following relation holds,

$$\mathcal{X}_{\text{es}} = \frac{\boldsymbol{P}_{\text{es}}}{\epsilon_0\boldsymbol{E}(\boldsymbol{r},t)}, \tag{2.4}$$

$\mathcal{X}_{\text{es}}$ being the dielectric susceptibility i.e. a measure of how polarized a material is when exposed to an x-ray photon, $\boldsymbol{P}_{\text{es}}$ being the polarization of the oscillating electron, which is related to the displacement, $\boldsymbol{x}(t)$, as $\boldsymbol{P}_{\text{es}} = -n_{\text{es}}q\boldsymbol{x}(t)$, where n_{es} is the electron charge density for a certain shell, s and ϵ_0 electric permittivity in vacuum. The usual notation for the complex refractive index is obtained by taking the ratio between the phase velocity of the x-ray photon in vacuum (c) and in the medium of propagation, v_{m}. However, by separating the real and the imaginary parts of the dielectric susceptibility, $\mathcal{X}_{\text{es}}$, the following relation holds,

$$n = \frac{c}{v_{\text{m}}} = \sqrt{1 + \mathcal{X}_{\text{es}}} \approx 1 - \delta_{\text{es}} + i\beta_{\text{es}}, \tag{2.5}$$

where δ_{es} and β_{es} are much less than unity for x-rays [11]. In equation 2.3 the electric field of the incident plane wave can be expressed as, $\boldsymbol{E}(\boldsymbol{r},t) = \boldsymbol{E}_{\text{incident}} \mathrm{e}^{-i(w_{\text{photon}} t - \boldsymbol{k}\cdot\boldsymbol{r})}$, which can be transformed into terms of the refractive index, n given the relation between the phase velocity and wave vector, $v = \frac{w_{\text{photon}}}{k} = \frac{c}{n}$ [12]. This means that a refracted x-ray photon in one dimension can be expressed as,

$$\boldsymbol{E}(z,t) = \boldsymbol{E}_{\text{incident}} \mathrm{e}^{-i(w_{\text{photon}} t - \frac{w_{\text{photon}} n}{c} z)}, \tag{2.6}$$

inserting refractive index into equation 2.6 gives

$$\boldsymbol{E}(z,t) = \boldsymbol{E}_{\text{incident}} \mathrm{e}^{-\frac{w_{\text{photon}} z \beta_{es}}{c}} \mathrm{e}^{i\frac{w_{\text{photon}} z}{c}(1-\delta_{es})} \mathrm{e}^{-i(w_{\text{photon}} t)}. \tag{2.7}$$

From equation 2.7 the effects of a refracted x-ray photon can be understood, where δ_{es} gives a phase shift to the incident x-ray photon and the complex part, β_{es} attenuates the wave, which can be further understood in Fig. 2.4.

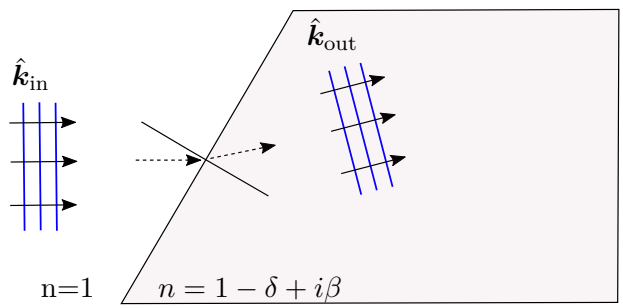

Figure 2.4: Incident plane x-ray photon first propagating in vacuum (n=1) with direction, $\hat{\boldsymbol{k}}_{\text{in}}$ until incident on a denser medium with refractive index, $n = 1-\delta+i\beta$. The refracted wave propagates in direction of $\hat{\boldsymbol{k}}_{\text{out}}$ and the electric field can be described by equation 2.7.

In reality different atoms contribute to the refractive index, hence to include all effects the contributions of all electrons add up to the dielectric susceptibility, $\mathcal{X}_{\text{eq}}$. Therefore, a more general notation of the refractive index is [11]

$$n = 1 - \sum_{n=1}^{q} \delta_{\text{es}} + i \sum_{n=1}^{q} \beta_{\text{es}} = 1 - \delta + i\beta. \tag{2.8}$$

Chapter 3

Polycapillary X-Ray Optics

This chapter describes the properties of the polycapillary optics and how they can be used to guide x-rays. It focusses mainly, on the theory that explains how x-rays can be guided, thus putting the main focus on total external reflection (TER), by using the refractive index and the theory obtained in chapter 2. Given the complex structure of the polycapillary optic, only a handful of equations are known. Some of these equations is stated as a guideline to validate measurements.

3.1 History and Basic Properties of Polycapillary Optics

The development of the polycapillary x-ray optics started by an idea that was somewhat different to x-rays, namely charged particles. The idea stated that high relativistic particles of energies around GeV such as protons could channel through crystals [13] and was predicted by Kumakhov. If channelling occurred the incoming charged particles would be aligned with a crystallographic axis, or planes causing the particles to be guided into a path called channels. Given that the particles where guided between planes the probability for direct collisions would decrease [14]. It was also found that bending the crystal would curve the channels creating the possibility to bend high energy charged particles. In 1976 Kumakhov also predicted a radiation of the channelled particles which later was experimentally verified by a group of scientist [15]. The channelling radiation from the charged particles, in the energy range from hard x-rays to gamma-rays was found at that time to be the most intense radiation among the present kinds, which led to an extensive use in diagnostics of crystals.

In 1979 Kumakhov was invited to the I. V. Kurchatov Institute of the Atomic Energy (IAE), which at that time was the worlds largest institute in Russia. Kumakhov accepted the invitation and left the Institute for Nuclear Physics in Moscow. At the new institution Kumakhov led a new project, which purpose was to achieve intense x-rays and gamma-rays with small divergences. The idea of channelling was thought as a solution to the problem by using the effects from the channelling

radiation. In 1980's an experiment was performed using the technique of channelling on a crystal. The crystal was a magnificent diamond of 1 cm in length named, "Valentina Tereshkova", in honor of being the first woman in space in 1963. The results from this diamond was great, however the radiation was produced by electrons in the range of GeV, which demands a large impractical accelerator. To be able to utilize this technique a new solution was necessary. The solution came at one of Kumakhovs sleepless nights in Minsk in the autumn of 1979 [16]. The solution arised from the known fact that x-rays could be reflected with minimal attenuation if the incident angle of the x-ray was less than the critical angle, θ_c or so called Fresnel angle [17]. This was discovered already in 1896 almost at the same time as W.C Röntgen in 1895 found the usefulness of x-rays [1]. Röntgen tried to verify this statement, but never succeeded. However, in 1927 Arthur H. Compton was rewarded the noble price in physics. At the Nobel lecture one of the concepts or experiments had proven that reflection can occur for x-rays as for natural light [18]. This meant that x-rays could be reflected, which led to Kumakhovs idea.

Kumakhov proposed that an optic could be constructed, consisting of channels likewise to the crystallographic channels, that would guide x-rays, but this time via total external reflection. The optic would then conduct the x-rays and perform multiple reflections on a curved structure, directing the x-rays into a small spot, thus focusing the beam to increase the flux density. Where flux density is the flux per unit area and this definition is used throughout the thesis.

It turned out that Kumakhov was right, x-rays could be guided by multiple reflection between two walls forming channels likewise to the channelling of charge particles. This was fascinating, what started as a way to guide charged particles ended up being useful for x-rays as well. This is today referred to as polycapillary optics also called Kumakhov optics and was formed in 1986 [19]. Since then over a decade of research has been put on the polycapillary optic and it is today used for all types of x-rays analysis [20]. However, aligning the polycapillary to a bright micro size spot, achieved by a liquid-metal-jet is a new area of research that could potentially set new limits for the polycapillary optic [4].

The polycapillary optic consist of small hollow glass tubes that each has a channel size of about 5-10 μm that are fused together using glue. The entire polycapillary optic is comprised of thousands to several million of these channels that are formed by heating and stretching larger glass tubes, that upon completion are cut and formed into hexagonal bundles that finally are fused together, which is demonstrated in Fig. 3.1.

The polycapillary optic is constructed such that each channel of the input of the polycapillary optic points towards the source spot. The channels are bent as seen in Fig. 3.1, such that they align to the same point, thus focusing the guided x-rays into one spot [21]. This means that the polycapillary optic functions as a waveguide similar to optical fibres. It collects the lower energy region of hard x-rays efficiently (< 40 keV) and then redirects them into a focused spot via total external reflection [20], seen in Fig. 3.2. Compared to other optics e.g. Montel optics [22], polycapillary optics collects the beam from thousands of channels and functions

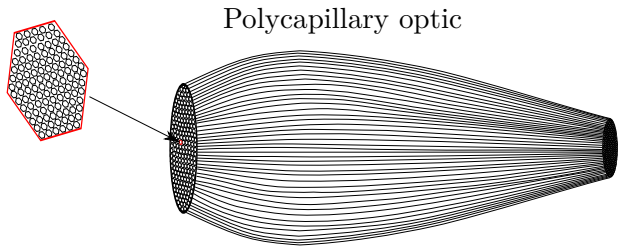

Figure 3.1: Polycapillary optic where the hollow glass tubes are bundled together forming a hexagonal structure, which can be seen at the input and output of the polycapillary optic. The upper left, red hexagonal is one bundle, which consist of several hollow glass tubes.

as a low pass filter, thus allowing lower energy x-rays to be directed, while higher energies are absorbed or not attenuated at all. The polycapillary optic is known to focus the x-rays into a virtual spot within ten's of microns, hence allowing a high flux density. However, achieving such a focused spot usually comes with the price of a higher output divergence.

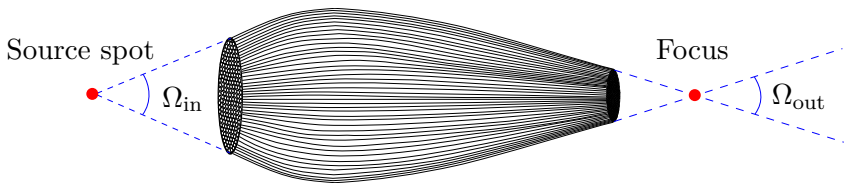

Figure 3.2: Sketch of how x-rays from the source spot are collected by the collecting angle, Ω_{in} and then guided by the polycapillary optic to form the output spot, having an output divergence, Ω_{out}.

3.2 Total External Reflection

Total external reflection occurs when incident wave is completely reflected, thus preserving the wave, but changing its direction of travel, somewhat as in coherent scattering described in section 2.1.2. This is fulfilled when the angle of incident, θ_{in} is smaller than the critical angle, θ_{c} [23]. To understand how this can be possible and for which incidents angles this is fulfilled, it is necessary to investigate the properties of the electric field as it interacts within the polycapillary optic.

Consider the state where the angle of incident $\theta_{\text{in}} > \theta_{\text{c}}$. Then a refracted and reflected wave is present after the point of interaction as in Fig. 3.3. By regarding the wave of incident as a plane wave and the interface of reflection as flat, the reflected and refracted waves will be plane as well. Furthermore, if the medium

of propagation is lossless, there will be no attenuation of the transmitted waves, implying the index of refraction, n is real, hence $n = 1 - \delta$ meaning that a phase shift occurs.

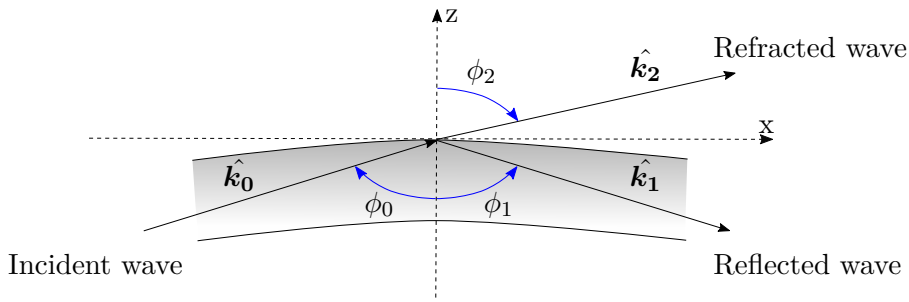

Figure 3.3: Incident plane wave at an angle relative the plane of incidence ϕ_0, interacts within one hollow capillary at z=0 and x=0. Afterwards two waves are transmitted, one reflected and one refracted, propagating in directions of $\hat{\boldsymbol{k}}_1$ and $\hat{\boldsymbol{k}}_2$ respectively.

Using the assembly as in Fig. 3.3. and the properties mentioned above, the electric fields of the three plane waves, E_{incident}, $E_{\text{reflected}}$ and $E_{\text{refracted}}$ can be expressed as,

$$\boldsymbol{E}_{\text{incident}}(\boldsymbol{r}, t) = \boldsymbol{E}_0 \mathrm{e}^{-i(w_0 t - \frac{w_0 n_0}{c} \hat{\boldsymbol{k}}_0 \cdot \boldsymbol{r}_0)}, \tag{3.1}$$

$$\boldsymbol{E}_{\text{reflected}}(\boldsymbol{r}, t) = \boldsymbol{E}_1 \mathrm{e}^{-i(w_1 t - \frac{w_1 n_1}{c} \hat{\boldsymbol{k}}_1 \cdot \boldsymbol{r}_1)}, \tag{3.2}$$

and

$$\boldsymbol{E}_{\text{refracted}}(\boldsymbol{r}, t) = \boldsymbol{E}_2 \mathrm{e}^{-i(w_2 t - \frac{w_2 n_2}{c} \hat{\boldsymbol{k}}_2 \cdot \boldsymbol{r}_2)}. \tag{3.3}$$

At the boundary, z=0, where the three waves meet, the fields (both electrical and magnetic field) must fulfil specific boundary conditions that obey Maxwell's equations [9]. The waves must be continuous for all times and positions on the boundary, implying that the exponential must match. Investigating this for the x-axis when $z = 0$, gives

$$\left[\mathrm{e}^{-i(w_0 t - \frac{w_0 n_0}{c} \hat{\boldsymbol{k}}_0 \cdot \boldsymbol{x})} = \mathrm{e}^{-i(w_1 t - \frac{w_1 n_1}{c} \hat{\boldsymbol{k}}_1 \cdot \boldsymbol{x})} = \mathrm{e}^{-i(w_2 t - \frac{w_2 n_2}{c} \hat{\boldsymbol{k}}_2 \cdot \boldsymbol{x})}\right]_{z=0}. \tag{3.4}$$

Equation 3.4 must be valid for all times, which means that the frequency of the three waves must be the same, implying that $w_0 = w_1 = w_2$ [24]. Without these time parameters equation 3.4 can be simplified to

$$n_0 \hat{\boldsymbol{k}}_0 \cdot \boldsymbol{x} = n_1 \hat{\boldsymbol{k}}_0 \cdot \boldsymbol{x} = n_2 \hat{\boldsymbol{k}}_0 \cdot \boldsymbol{x}. \tag{3.5}$$

Using Fig. 3.3 the unit wave vectors in the x direction can be written in terms of sinus functions,

$$n_0 \sin\phi_0 = n_1 \sin\phi_1 = n_2 \sin\phi_2. \tag{3.6}$$

Noting that the incident and the reflected wave is in the same medium i.e. $n_0 = n_1$ and using this fact the following relations holds

$$\phi_0 = \phi_1, \tag{3.7}$$

the reflected wave is reflected into the angle of incident and the refracted wave is related to

$$n_0 \sin\phi_0 = n_2 \sin\phi_2. \tag{3.8}$$

It is now interesting to see what happens when the condition for total external reflection is fulfilled and for which angles of incident that this is satisfied. By assuming that the incident x-ray propagates in vacuum ($n_0 = 1$) and that the medium is lossless equation 3.8 can be rewritten

$$\sin\phi_2 = \frac{\sin\phi_0}{n_2} = \frac{\sin\phi_0}{1-\delta_2}. \tag{3.9}$$

Remembering from section 2.1.3, δ is usually positive and much less than unity for x-rays. Then the following relation must hold

$$\phi_2 > \phi_0 \tag{3.10}$$

Recall Fig. 3.3, by letting $\phi_0 \to \frac{\pi}{2}$, then $\phi_2 \to \frac{\pi}{2}$ faster than ϕ_0. Total external reflection will begin to appear when $\phi_2 = \frac{\pi}{2}$, keeping equation 3.10 in mind the condition for total external reflection can be inserted into equation 3.9, giving

$$\sin\frac{\pi}{2} = 1 = \frac{\sin\phi_c}{1-\delta_2} \longrightarrow 1 - \delta_2 = \sin\phi_c, \tag{3.11}$$

were ϕ_c is the critical angle relative, the plane of incidence. Using that only small angles are directed equation 3.11 can be rewritten using Maclaurin expansion for $\sin\phi_c$ with respect to ϕ_c and relating the critical angle to the incident wall as in Fig. 3.4 ($\theta_c = \frac{\pi}{2} - \phi_c$), the condition for fulfilling total external reflection is obtained

$$\theta_c = \sqrt{2\delta_2}. \tag{3.12}$$

This gives a solid understanding of the condition for TER, $\theta_{in} \leq \theta_c$. However, if the material is known, equation 3.12, can be transformed into a more suitable relation with the following expression [6]

$$\delta_2 = \frac{r_e h^2 c^2}{2\pi E^2} \sum_{i=1}^{n} n_z f_{1Z}^0(E), \tag{3.13}$$

where $r_e \approx 2.82 \cdot 10^{-15}$ m is the classical electron radius, $h \approx 4.14 \cdot 10^{-15}\ eV \times s$ Planck's constant [25], n_z number of atoms per volume of a specific element Z, f_{1Z}^0 the forward scattering factor, which approaches the atomic number, $f_{1Z}^0 \approx Z$, for

energies above the electron binding energies. The sum is calculated for all present materials, n with atomic number, Z. Using this relation for δ_2, gives

$$\theta_c = \sqrt{\frac{r_e h^2 c^2}{\pi E^2} \sum_{i=1}^{n} n_z f_{1Z}^0(E)} \approx \sqrt{\frac{r_e h^2 c^2}{\pi E^2} \sum_{i=1}^{n} n_z Z}. \tag{3.14}$$

In this case the polycapillary consist of borosilicate glass, which can have several different composition [26], but for polycapillary optics equation 3.14 can be simplified to [23]

$$\theta_c \approx \frac{30\ [\text{keV}]}{E} [\text{mrad}], \tag{3.15}$$

thus the higher the energy the smaller the critical angle is, hence the polycapillary optic guides fewer and fewer x-rays as the energy increase.

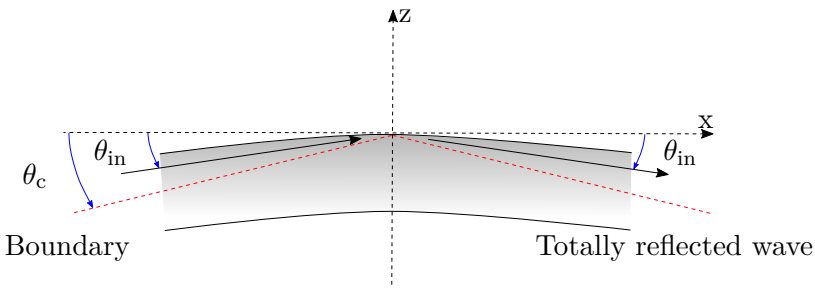

Figure 3.4: Total external reflection satisfied when $\theta_{in} \leq \theta_c$, thus below the red boundary.

3.3 Input Focal Distance

The input focal distance (IFD) usually denoted f_1 is the distance from the source spot to the input of the polycapillary optic, when it guides as many photons as possible, with a collecting angle denoted Ω_{in} as in Fig. 3.2.

3.4 Output Focal Distance

The output focal distance (OFD) usually denoted f_2 is the distance measured from the output of the polycapillary optic to its focus. The distance depends on the curvature of the polycapillary optic, thus the more bent the capillaries are the shorter the OFD will be. This distance is for many users crucial in order to perform measurements, since a too short OFD will leave no room for equipment that is essential for the measurement. At the focus the photons will converge with an convergence angle, Ω_{out} see Fig. 3.2.

3.5 Output Divergence and Pointing Direction of Polycapillary Optic

The output divergence, or simply convergence angle of the polycapillary optic, can be divide into two parameters: global divergence $\alpha = \Omega_{\text{out}}$ and local divergence β as shown in Fig. 3.5. The global divergence, α is determined by the output diameter D_{out} of the polycapillary optic and the OFD, according to $\alpha = 2\tan^{-1}(\frac{D_{\text{out}}}{2\text{OFD}})$. Having a shorter OFD will direct the x-rays into a smaller spot and increase the global divergence. A less divergent output allows for a more pencil like beam with larger depth of focus, realizing less variation of the spot. This results in a beam that is less sensitive yielding more accurate measurements.

The local divergence, β of each capillary is in principle determined by the critical angle, θ_{c} for a large source. So for a large x-ray source the output divergence is $\beta = 2\theta_{\text{c}}$.

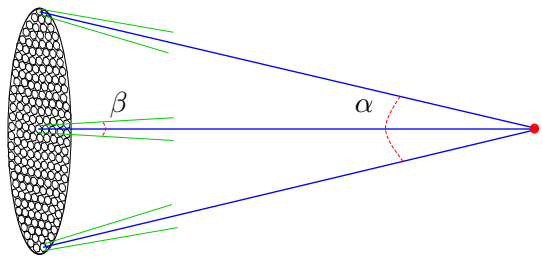

Figure 3.5: Global, α and local, β divergence of the output of the polycapillary optic.

An important concept, is that each capillary contributes to the effective spot. This means that each capillary can be considered to produce a Gaussian beam, where the FWHM depends on the local divergence and the effective spot is the net effect from all Gaussian beams generate from each capillaries. If all the capillaries are perfectly aligned the minimum spot size is achieved and will be determined by the local divergence according to equation 3.17 in section 3.6.

3.6 Spot Size

The spot size (focus spot size) is the diameter of the focused spot. For many applications the spot size is preferred to be as small as possible in order to focus and investigate the structure in micro to nano scale as seen in Fig. 3.7. By using the known properties about the polycapillary optic above, it is expected that the spot size is to be dependent on the OFD and the critical angle, θ_{c}. Having a shorter OFD will induce a more variable spot size when scanning over a rough sample due to the larger divergence, which is illustrated in Fig. 3.7. By considering one capillary it is possible to derive a relation for the spot size see Fig. 3.6. From Fig. 3.6. the

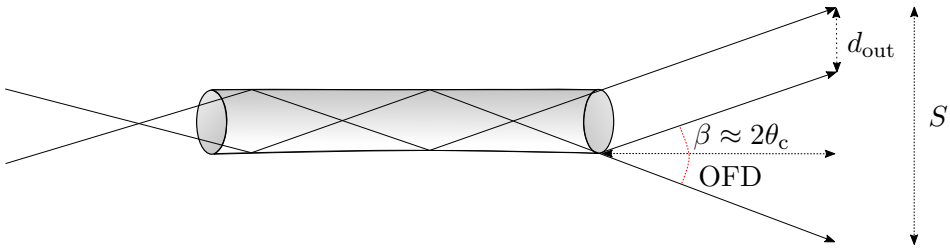

Figure 3.6: Focus size, S dependence on OFD, β and the diameter of the capillary, d_{out}.

focus spot size approximately follows

$$S = 2\text{OFD}\theta_c + d_{\text{out}}, \tag{3.16}$$

where d_{out} is the capillary diameter of one hollow tube, which is usually much less than the spot size, and therefore neglected. Remember the relation for the critical angle relative the energy i.e. equation 3.15. Using that relation in equation 3.16 yields

$$S\ [\mu m] = \frac{60\text{OFD}\ [\text{mm}]}{E\ [\text{keV}]}. \tag{3.17}$$

Equation 3.17 is a fundamental property of the polycapillary optic and the same analogy holds for the input of the polycapillary optic, but where the source size, S, is fix. The critical angle decreases as the energy increases, yielding a smaller spot. The amount of x-rays that reflects through the polycapillary optic will decrease relative the critical angle, which means that higher energies results in lower flux through the focus. Furthermore, decreasing the OFD will minimize the spot size, however making the polycapillary optic more impractical in terms of space to the sample and output divergence.

These parameters are all essential when designing the polycapillary optic and the observed spot size will be the net sum of the contributions from all energies. Prioritising a small spot gives a better accuracy, but on the other hand less flux. Another important factor compared to achromatic optics is the varying spot size for different energies [27].

Fig. 3.7 is an example of an XRF analyse on a skin sample, that illustrates the difficulty in keeping a small spot size when the convergence angle, α, is big.

Since the polycapillary optic in Fig. 3.7 sits at a fix position, due to the complexity to move the source, the samples moves through the beam. Since the surface of the sample being uneven the distance to the sample will vary (Δx) and so the spot size. The smaller spot reduces the effective area that the x-rays interacts with, giving higher resolution.

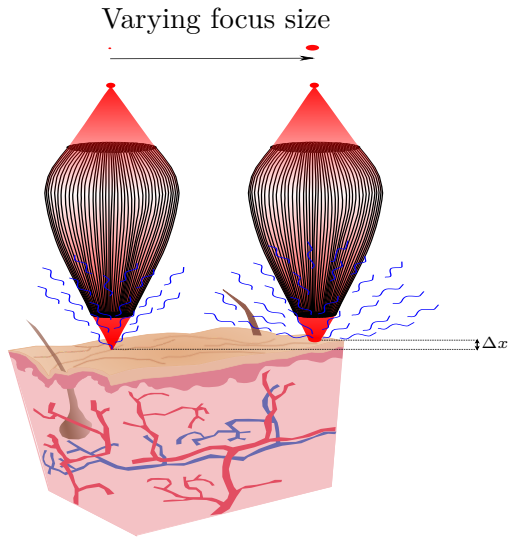

Figure 3.7: Using the polycapillary optic to scan over a sample that moves, in this case the top of a skin sample. The left position of the polycapillary optic hits the sample at OFD, while the right x-rays hits the sample before reaching the focus, hence the difference Δx between the two positions.

3.7 Beneficial Predictions of Aligning the Polycapillary Optic to a Micro Focus Source

As mentioned there is nothing new by guiding x-rays with polycapillaries. However, previously conducted measures have been executed with larger spots that theoretically aren't as beneficial as having a small source spot with the same electron beam power. Larger source spots, increase the amount of photons that incident at greater angles, resulting in a larger spot according to equation 3.16.

For smaller spots, less photons are incident on great angels, which can make the local divergence less than twice the critical angle, resulting in a smaller focus according to Fig 3.8. However, having a smaller source spot could induce other parameters that could affect the spot size, one of these being the pointing direction of the output capillaries.

A well defined focus is achieved when the ends of the capillaries points in the same direction. When designing the polycapillary optic it is most likely that this criteria remains unfulfilled. However, for a large source spot the amount of photons at larger angles will be higher, resulting in a larger local divergence that could smear out the effects of uneven pointing directions. For a small source spot the case is different. As mentioned smaller source spots will have less photons at greater angles causing a smaller effective spot. However, the local divergence of each capillary could be so small that a slight offset in the ends, could increase the effective spot size.

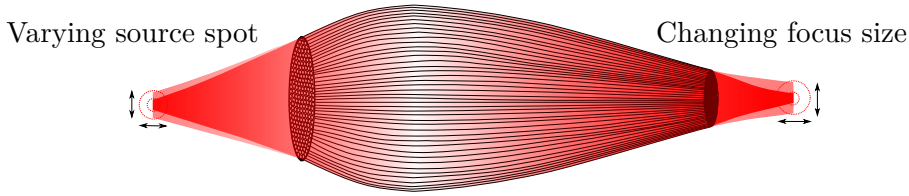

Figure 3.8: Variation of the source spot size should change the output focus size.

This would mean that even if each capillary achieves a small spot the effective spot achieved by all capillaries, could be significantly larger, due to different pointing directions. This can be understood further from Fig. 3.9, where a comparison is made between capillaries pointing in the same direction and capillaries that points in a more random direction causing a wider focus.

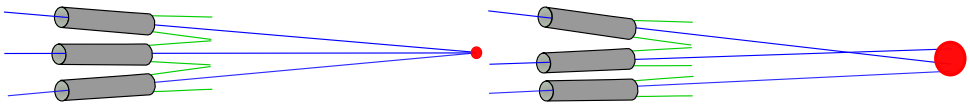

(a) No offset (b) Offset

Figure 3.9: Both (a) and (b) contains three capillaries that represent the capillary in the middle of the polycapillary optic and the two outermost relative the center of the polycapillary optic. (a) Shows the optimal design of the polycapillary optic, where the ends of the capillaries points in the same direction. (b) Represents a slight offset between the capillaries causing a wider focus.

Furthermore, a small source spot would in theory induce a higher gain. The gain is calculated as ratio between the flux density, through the focus, with and without the polycapillary optic. Where flux density is the flux per unit area, $\Psi = \frac{\psi}{\mathrm{A}}$, where A is the area of interest and ψ the flux through that area.

During measurements, the detector was not positioned in the focus, but knowing the OFD and by treating the source distribution symmetrically, thus using the relation for the solid angle, $\Omega = \frac{\mathrm{A}}{r^2}$, where r is the distance from the source to the focus it is possible to extract the flux density at the focus. The flux density at the focus, can be written as

$$\Psi_{\mathrm{focus}} = \frac{\psi_{\mathrm{focus}}}{\mathrm{A}_{\mathrm{focus}}}, \tag{3.18}$$

and the flux density measured at detector, positioned $x_{detector}$ from the focus can be written as

$$\Psi_{\mathrm{detector}} = \frac{\psi_{\mathrm{detector}}}{\mathrm{A}_{\mathrm{detector}}}, \tag{3.19}$$

where $A_{detector}$ is the area of the detector. Using the fact that the solid angle Ω, must be the same at the position of the detector and at focus when the polycapillary

optic not is inserted, it is possible to write

$$\frac{A_{\text{detector}}}{(r + x_{\text{detector})^2}} = \frac{A_{\text{focus}}}{r^2}, \tag{3.20}$$

also the flux measured at the detector will be the same as the one measure in focus, $\psi_{\text{focus}} = \psi_{\text{detetor}}$ with the exception that the detector captures all photons, using this gives

$$\Psi_{\text{focus}} = \frac{\psi_{\text{focus}}}{\text{A}_{\text{focus}}} = \frac{\psi_{\text{focus}}(r + x^2_{\text{detector}})}{A_{\text{detector}} r^2}, \tag{3.21}$$

However, when the polycapillary optic is inserted it is possible to extract the area of focus from the knife edge scan using the FWHM, which yields the final expression for the gain used within this thesis

$$\text{Gain} = \frac{\frac{\psi_{\text{focus with optic}}}{\text{A}_{\text{focus with optic}}}}{\frac{\psi_{\text{focus without optic}}(r+x^2_{\text{detector}})}{A_{\text{detector}} r^2}}, \tag{3.22}$$

where the area of focus with the polycapillary optic is written as $A_{\text{focus with optic}} = \pi(\frac{\text{FWHM}}{2})^2$.

A smaller source spot should increase the transmission through the polycapillary optic, since less photons are incident at greater angles, causing a larger numerator when calculating the gain. Furthermore, a smaller source as previously mentioned, should change the focus size, also contributing to a higher gain.

3.8 Halo Effect and Undesirable Properties

Previously, section 3.2 has investigated the condition for when total external reflection is satisfied. However, if the energies of the incoming x-rays are too high, it doesn't matter how small the incident angle is, the x-rays will penetrate straight through the polycapillary optic. The penetration of the polycapillary optic is usually referred to as the halo effect, which increases the high energy background, that could smear out the beam profile. This is generated by two types of penetration, either origination from high energy x-rays or from low energy x-rays. Penetration of high energy x-rays is usually handle by keeping the energy of the incident x-rays under 40 keV [20]. This could also be decreased by increasing the length of the polycapillary optic, thus increasing the absorption within each capillary.

The penetration of low energy x-rays arises when the angle of incidence is above the boundary for the critical angle. In that case the x-ray could either be absorbed, or a refracted ray could arise as in Fig. 3.3. The refracted ray could then be absorbed by other capillaries. However, if this occurs near the output where there is less capillaries, there is a chance that the ray escape the polycapillary optic. Controlling this could possibly be done by change the composition of the polycapillary optic, which would change δ as previously described in section 2.1.3, that in turn

would change the critical angle, θ_c seen by equation 3.12. Both of these penetration effects could smear out the sharp focus, but usually the effect of halo is far less than the x-rays that are guided and therefore usually negligible.

Another important factor is the design of the polycapillary optic. The polycapillary optic must be constructed with high accuracy thus making it possible to create several lenses that delivers roughly the same precisions, which today is possible. However, there can always appear small deviations. Most likely is a broken capillary where the walls have fallen down, thus interfering with incoming x-rays and changing the properties of the lens. There could also arise a certain waviness to the walls of the polycapillary optic, which would change the amount of x-rays that are reflected, thus changing the spot size and flux properties. These types of undesirable properties can usually be seen by an image of the polycapillary optic. Capillaries with lower performance will simply yield lower flux.

Chapter 4

X-Ray Sources

Most common x-ray sources are based on having free electrons accelerated to great speeds (around 30-65% of the speed of light for medical applications [28]) and thereafter aligned into a metal target that produces x-rays during the interaction. The sources utilizing this technique are called electron-impact x-ray sources, or simply x-ray tubes, which are based on the same principle as the one Röntgen used [1]. Newer techniques have been developed, such as free-electron lasers and synchrotron's, however they require large expensive facilities, whereas electron-impact sources are relativity small (less expensive), with enough performance for most applications. This chapter describes the basics behind electron-impact sources such as: interaction processes in the target and the characteristic emission spectrum that the polycapillary optic is exposed to, where the main focus will be on the liquid-metal-jet source that is used within this thesis.

4.1 Electron-Impact X-Ray Sources

Electron impact x-ray sources are based on a vacuum tube, or more known as x-ray tube in which electrons are accelerated, as seen in Fig. 4.1. Free electrons are generated by heating a small filament located at a negatively charge side of the tube (cathode). Once ejected they are accelerated by an electric field generated by an external high voltage difference between the two ends of the tube, ranging from tens to several hundreds of kilovolts [6]. During the acceleration, electrons are aligned using electromagnets that directs them into a spot on the target, which usually consist of metal. At the boundary of interaction, or simply at the anode two process in which x-rays are produced appears.

The first process, is similar to the photoelectric effect as in section 2.1.1 but in which an electron ionizes an atom of the target. This process is refereed to as characteristic line emission, since the radiation is characteristic for the specific atom. As seen in Fig. 4.2 , after ionisation another electron from a higher electron shell will fill the empty spot. While doing so the electron from the higher shell

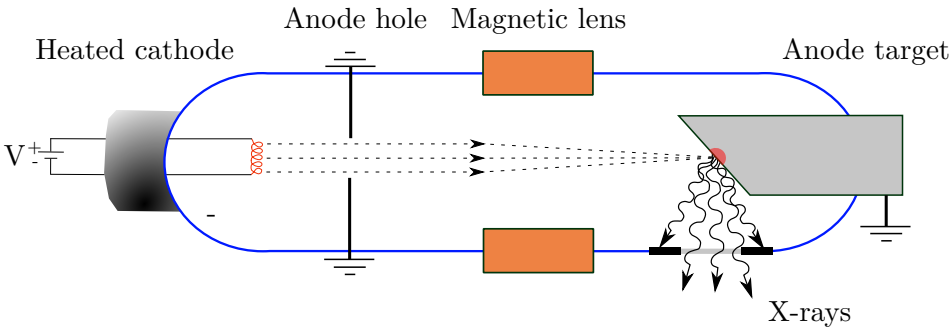

Figure 4.1: X-ray tube, where the blue boundary is the region of vacuum to which the electrons are accelerated by an external electric field between the cathode and the anode. The potential difference on the left side controls the heating of the cathode, thus controlling the emission current. The anode hole blocks divergent electrons, narrowing the beam width. The magnetic lens aligns the electron beam into a small spot on the anode, where the red area is locally heated. Interactions at the anode produces x-rays in all directions, but only illustrated against the exit window.

will go from a higher energy state, or simply not as bound, to a more bound state with lower energy where the surplus of energy is emitted as a photon. These x-rays are related to the energy difference of the shells, which is specific for each elements and usually electrons from the L and M shell fills the hole refered to as K_α and K_β transitions respectively. The material of the liquid-metal-jet anode used within this thesis is referred to as Exalloy G1, which is mainly composed of gallium and a small amount of indium to reduce the melting temperature [4]. Gallium has a K_{α_1} line at an energy of 9.3 keV and indium has an K_{α_1} at 24.2 keV and both atoms has an K_{α_2} emission approximately at the same energies [29]. Furthermore, Gallium has a $K_{\beta_{1,2,3}}$ close to 10.3 keV and Indium has a $K_{\beta_{1,2,3}}$ near 27.3 keV. These emissions lines are the peaks seen in the spectrum of Fig. 4.3 [30].

The second process, bremsstrahlung, or braking radiation appears when an incoming electron passes near to an atomic nucleus as seen in Fig. 4.2 (b). The nucleus being positively charged, results in a present electric field that will deccelerate the electron when passing according to the Lorentz force, $\boldsymbol{F} = q\boldsymbol{E}$, where q being the charge of the passing electron and $\boldsymbol{E}$ the electric field. During the deccelleration, the kinetic energy of the electron decreases and is transferred into emission of a photon. The most intense x-ray is produced when the incident electron is stopped, thus transferring all of its energy. Since different electrons interacts differently with the electric field a continuous spectrum of photons is emitted, which is seen as the slow varying part in the spectrum in Fig. 4.3 [6]. Bremsstrahlung radi-

ation is therefore correlated to the incident electron energy, but also to the atomic nucleus. Higher atomic numbers has a stronger net charge of the nucleus giving a stronger electric field that can stop the incoming electrons faster. Therefore, usually high atomic numbers are used to extract the most of the incoming energy, but even with high atomic numbers as tungsten and an acceleration voltage around 100 kV the efficiency is as low as about 1% [31].

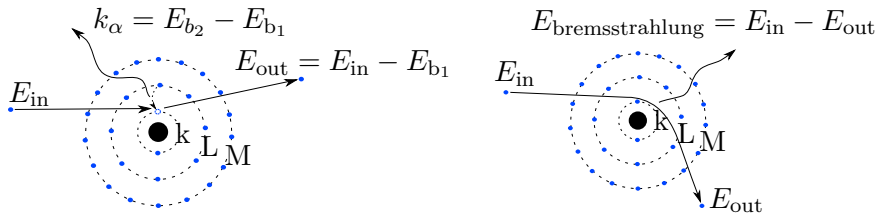

(a) Characteristic line emission (b) Bremsstrahlung

Figure 4.2: (a) In characteristic line emission an incident electron with energy E_{in}, knocks out an electron from the inner shell K, with binding energy E_{b_1}. The empty vacancy is filled by electrons from higher shells, in the figure from the second shell, thus k_α radiation is emitted. (b) In bremsstrahlung radiation an incident electron accelerates by the electric field from the atomic nucleus in which the electron losses energy, in form of radiation.

Fig. 4.3 shows the x-ray emission spectrum for the MetalJet D2+ that the polycapillary optic is exposed to throughout this thesis.

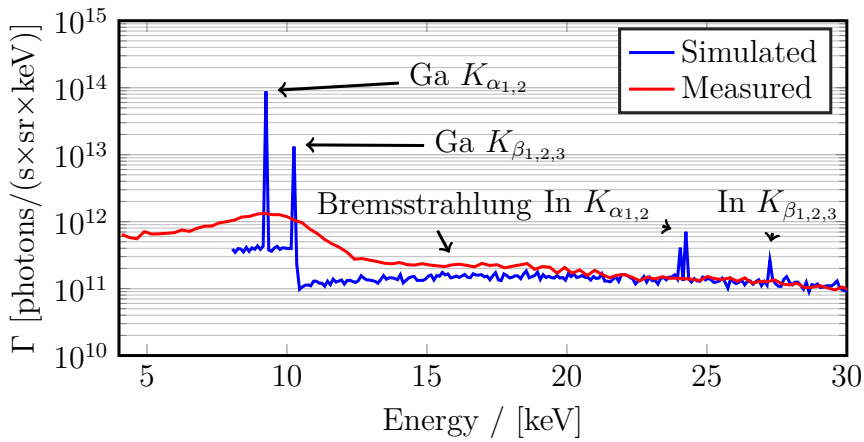

Figure 4.3: Simulated versus measured x-ray emission spectrum, plotted for the settings on the source, where the liquid-metal-jet had a 70 kV acceleration voltage and a spot size of 20 μm on 260 W for Exalloy G1. Due to poor energy resolution of the detector the Ga k_α and Ga k_β peaks appears as one wide peak.

The measured data is compensated for the reduced detection efficiency of the detector at higher energies, this using attenuation coefficients from NIST [32]. There is a slight difference between the two curves in Fig. 4.3. The Ga k_α and Ga k_β peaks of the measurement appears as one wide peak compared to the simulation. This is due to the poor energy resolution of the detector used. However, by integrating both the Ga k_α and Ga k_β peak for the simulation ($\Phi = \int_{E_{\text{peaks}}} \Gamma \, dE$) and comparing their sum against the integral of the wider peak from the measured spectrum, gives the same amounts (i.e. $\Phi_{\text{measured}} = \Phi_{\text{simulated}} \approx 5 \cdot 10^{12} \ \frac{\text{photons}}{\text{s} \times \text{sr}}$).

While the two curves align well for higher energies there is a small difference in the energy region of 10 keV$\leq E \leq$20 keV. This difference is most likely caused by two lower energy photons that reaches the detector at the same time, where the detector interprets them as one photon with the sum of their energies. Fortunately, the probability for this is low but still noticeable. The peaks for higher energies, are not as visible. This is due to the poor resolution and slight transmission through the detector (not all photons are absorbed), that increases with energy.

4.2 Liquid-Metal-Jet Sources

An issue limiting the brightness for electron impact x-ray sources is the heat load at the anode. Even though the energy of the incoming electrons is dissipated via the two process mention in section 4.1, there is a lot of energy that transforms into heat. Over 99% of the incoming electron beam energy imparted on the anode turns into heat [33]. The heat dissipated at the anode must quickly be transported away in order to not damage the anode. During the years several ways to maximize the power without melting the anode has been implemented, such as improving the heat dissipation.

First, by making the anode slightly angled as seen in Fig. 4.4 . This will reduce the effective area from which the x-rays are emitted from compared to the area of which the electron beam interacts with, thus causing the energy to spread out. Secondly, choosing a material with high atomic number to maximize generation of bremsstrahlung while still having a high melting point and still producing characteristic x-rays that are relevant for the application. Last, implementing a rotating anode will spread out the energy and in that way increase the maximum power load.

Today there is not much room or tricks left for improvement for the rotating anode, the maximum power load has been reached. However, in the last decade the new concept of a liquid-metal-jet anode was invented, that started at the Biomedical and X-ray Physics group at KTH and has today formed the company, Excillum [3]. The jet can reach speeds of about 70 m/s. This allows for a regenerative anode that efficiently can transport the heat away, thus increasing the power loading. Since the anode already being melted it also meant that the material could be loaded over its damage point also increasing the power load. The jet technique also implied a smother target compared to the rotating anode. This allowed for smaller spot size,

in the range of 5 to 20 μm, with a power loading up to 260 W. This power loading is in the order of thousands of GW per area. The flux achieved is roughly ten times higher compared to a conventional solid anode from sources with the same spot size, but is continuously being improved [3]. Fig. 4.4. Shows the benefit of having a liquid-metal-jet compared to a rotating anode.

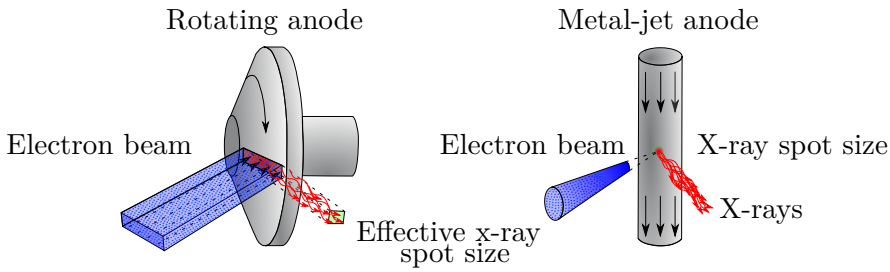

Figure 4.4: Electron beam (blue) incident on a rotating anode and a metal-jet anode. In reality x-rays are generated around all directions at the anode, which is hard to illustrated and therefore only a small subset of x-rays are shown. X-rays generated from the rotating anode appears to come from the green effective area, but comes in fact from the red area due to the angled anode. X-rays generated from the liquid-metal-jet are more compact, thus achieving a higher brightness compared to the rotating anode. The liquid-metal-jet also transports heat away efficiently as the rotating anode, but also having the benefit of being self regenerative, thus repairing eventual damages. Figure adapted from [6].

The source used within this thesis is called MetalJet D2+, set to have a spot size of roughly 20 μm seen in Fig. 4.5, on 260 W and a 70 kV acceleration voltage if not otherwise is stated.

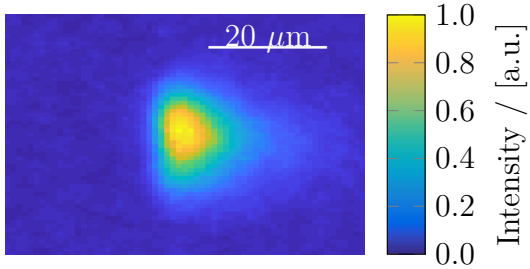

Figure 4.5: Liquid-metal-jet source spot on 20 μm with 260 W and 70 kV acceleration voltage.

Chapter 5

Outline of Measurement

One of the essential tools in characterising the performance of the polycapillary optic relates to the technique used to detect photons form the polycapillary optic. The method of choice should foremost be able to determine spot size and flux with high accuracy and precision. A method fulfilling these qualities is the so called knife edge scan, which is the method used throughout this thesis. The detector used for the knife edge scan, counts individual x-ray photons and has the benefit of discriminating photons, thus allowing to measure photons within a certain energy span. This chapter will present an overall setup of the polycapillary optic as seen in Fig. 5.1. The focus, however will be on the properties of the knife edge scan and how it is used to determined design parameters of the polycapillary optic such as OFD.

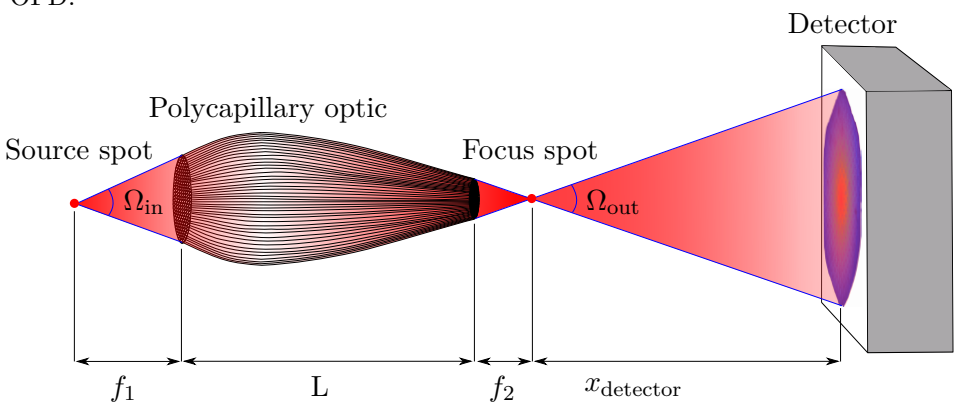

Figure 5.1: The polycappillary optic with length L aligned to a source spot located at IFD f_1 with an input divergence Ω_{in}. The output of the polycapillary optic has a divergence of Ω_{out} where the focus is located at OFD f_2. The x-rays are captured by the area of the photon-counting detector placed at a distance x_{detector} from the focus spot.

5.1 Knife Edge Scan

By continuously inserting a thin (sharp) plate perpendicular to the beam as in Fig. 5.2, it is possible to determine the beam width (FWHM) at different positions, specifically at the focus, but also where the center of the beam lies. The scan can proceed both in horizontal and vertical directions, refereed to as $\hat{x}$ and $\hat{y}$ respectively throughout this thesis. This allows for the characterization of the performance of the polycapillary optic in two dimensions.

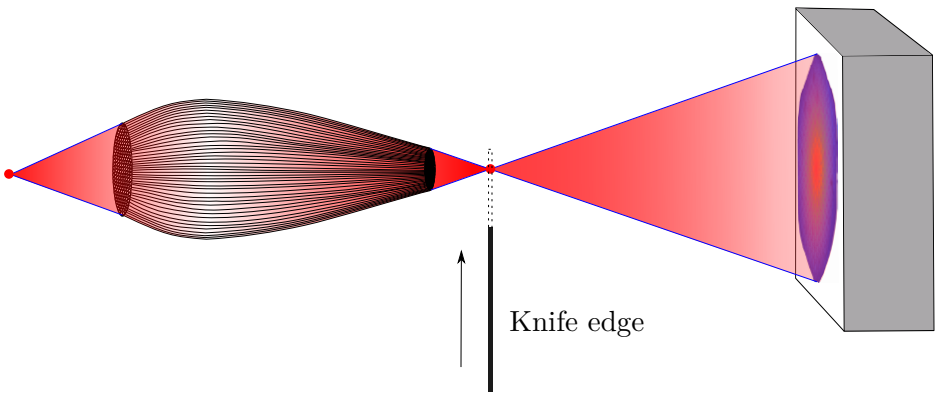

Figure 5.2: Knife edge scan.

This is manageable if the sharp edge is thin, while still being able to fully absorb the incoming photons. The knife edge needs to be thinner than the depth of focus of the polycapillary optic, in order to find the focus with high accuracy. This since the focus will appear for the smallest waist rather than a point as in classical optics. Therefore, the knife edge was designed using equation 2.1 to be as thin as possible while still having enough thickness to absorb incoming photons. The final edge consisted of a tungsten foil with a 50 μm thickness.

As the knife edge steps through the beam an edge-spread function (ESF) can be obtained, from which the characteristics of the beam can be gained, shown in Fig. 5.3. To obtain the ESF and get the true spot size one should sum the entire detector for each position of the knife edge. The result will be the cross sectional profile of the response to an edge shaped signal [11]. For a Gaussian focus, the obtained curve can be approximated as an error function for which it is possible to do a numerical fit according to

$$\psi = \psi_0 + \frac{\psi_{\max}}{2}(1 - \mathrm{erf}(\frac{x - x_{\mathrm{center}}}{\sigma\sqrt{2}})), \tag{5.1}$$

where ψ_0 is the background offset flux, $\psi_{\max}$ is the maximum flux present without the knife edge, x_{center} is the position of the shift (inflection point), σ is the standard deviation and erf is the error function. Solving equation 5.1 in the least square

sense with proper start guesses, gives the unknown parameters, ψ_0, $\psi_{\max}$, x_{center} and σ. From these parameters the FWHM of the corresponding Gaussian can be calculated, according to

$$\text{FWHM} = 2\sqrt{2\ln(2)}\sigma. \tag{5.2}$$

Notice that considering the photons measured per pixel instead of the total sum of all pixels, allows for separate edge spread functions for all pixels. This means that valuable information about FWHM and the center (x_{center}) can be obtained for different parts of the polycapillary optic.

While the edge spread function is a solid way to determine FWHM and the inflection point, there is a more visual method. This method allows a beam profile, instead of an knife edge scan profile. The beam profile can be extracted from the ESF as

$$\text{LSF}(x) = \frac{d\text{ESF}(x)}{dx}, \tag{5.3}$$

where the movement of the knife edge is in the horizontal x direction and LSF, the line spread function, which can be seen in Fig. 5.3. The LSF will appear as a Gaussian function, from which it is easier to see the FWHM and the center. However, taking the derivative of the ESF can induce noise making the result of the LSF less accurate.

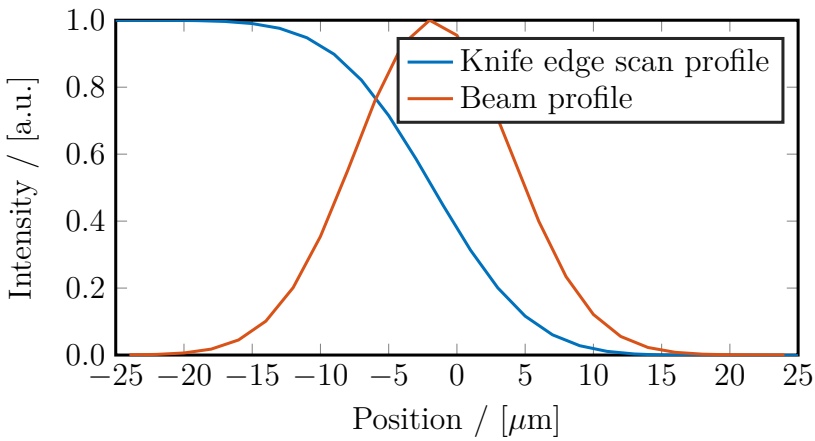

Figure 5.3: Edge spread function (ESF) versus line spread function (LSF).

5.2 Detector

The detector used is developed by X-spectrum, photon-counting with a 300 μm thick silicon sensor, based on the Medipix3 chip, thus allowing two energy thresholds. The detector has different running modes with a maximum of 24 bit for one

energy threshold, and 12 bit when using two energy thresholds. In order to avoid saturation the 24 bit mode was used, however by using the fact that the source is constant over time one could set different single energy thresholds and then subtract the data to get the result achieved when using two energy thresholds. The detector consist of $256 \times 256 = 65536$ pixels, with a pixel size of 55 μm, giving a total detector area of 14×14 mm^2 $= 196$ mm^2 [34].

5.3 Alignment of Polycapillary Optic

The polycapillary optic is mounted on a motorized stage (actuator) that allows for μm movements in the x, y and z direction and was developed by ZABER of series T-LA28A [35]. In order to achieve optimal performance it is of most importance that the polycapillary optic is well aligned against the liquid-metal-jet. The section section will state the techniques used to align the polycapillary optic and the gained results.

5.3.1 Rough Alignment

First, a rough alignment was done where the polycapillary optic was mounted at larger than nominal displacement from the source (in z direction) and a throughput of the polycapillary optic was observed while moving the stage. This was either done using the photon-counting detector and a PIN diode. The PIN diode was only used to verify the measurements of the photon-counting detector, due to the superior benefits of the photon-counting detector.

5.3.2 Final Accurate Alignment

Secondly, once the rough alignment in x, y and z space was conducted the optimal alignment towards the source could start, finding the IFD in the z-direction. This could be done by manually moving the lens in z direction by using a feeler gauge and for each movement recording a net current or an image at the photon-counting detector. By plotting the normalized total flux the IFD could be found. However, with the imaging detector it was possible to validate these result from the image at the detector. The technique for this "visual" alignment is illustrated in Fig. 5.4-5.5, were the scales are exaggerated.

In Fig. 5.4 the source spot is place behind the IFD (f_1), thus being too far away from the polycapillary optic. To see if the lens is in this state, it was moved with the motorized stage holding the lens in the direction according to Fig. 5.4. After a certain movement, only half the polycapillary optic will guide x-rays efficiently due to the condition of TER, given the position of the source relative the polycapillary optic. Since only half the polycapillary optic is active the image of the detector will be intenser at one side relative the other as seen in Fig. 5.4. Therefore, a movement in the direction according to Fig. 5.4 will yield an image that disappears in the opposite direction to the movement of the polycapillary optic.

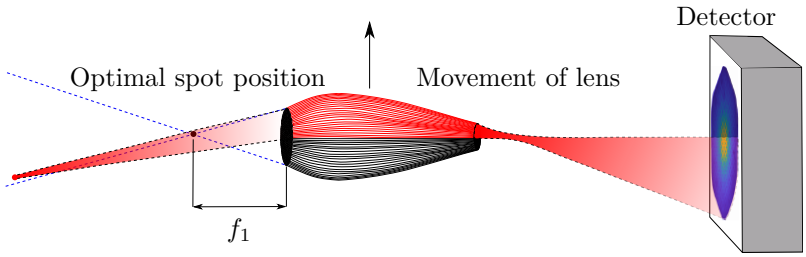

Figure 5.4: Source spot aligned too far away from the lens, thus behind the IFD (f_1). Only the top half of the polycapillary optic functions in a desired way, when the polycapillary optic is moved upwards from best alignment, marked in red.

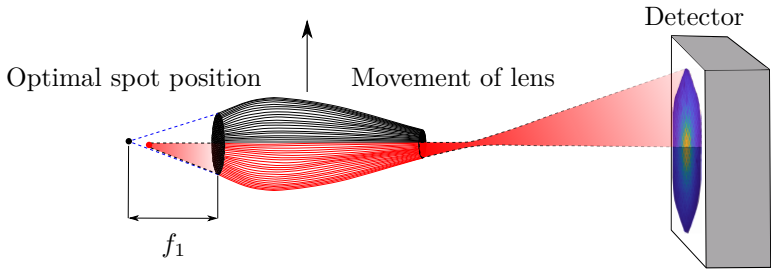

Figure 5.5: Source spot aligned too close to the lens, thus in front of the IFD (f_1). Only the bottom half of the polycapillary optic functions in a desired way, when the polycapillary optic is moved upwards from best alignment, marked in red.

In Fig. 5.5 the source is placed in front of the IFD (f_1) i.e opposite to the state in Fig. 5.4. Moving the polycapillary optic in the same direction as in Fig. 5.4 results in the opposite effect, thus the image disappears in the direction of the movement.

When the source spot is centred at the IFD and the lens is moved horizontally (x direction, same as above) each pixel will lose intensity equally much as illustrated in Fig. 5.6.

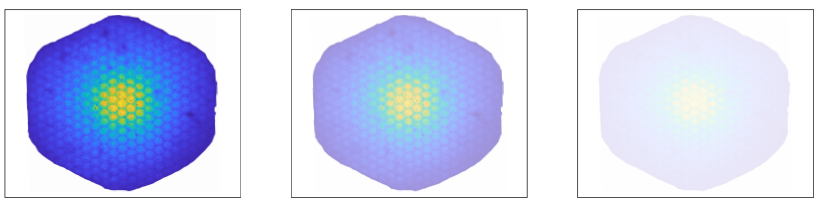

(a) (b) (c)

Figure 5.6: Images (a)-(c) shows how the intensity decreases as the motorized stage translates the lens, when the source spot is placed at IFD.

When the position in z direction is found, as in Fig. 5.6, the lens is moved in x and y direction in order to maximize the flux.

5.3.3 How to Find OFD

The focus, or the OFD, can be found using the knife edge. Scanning through the beam for different z positions and plotting it against the FWHM, gives the location of the focus. Starting to scan near the output of the polycapillary optic and stepping further away will decrease the FWHM until the focus is passed, from which the FWHM start to increase. This means that the smallest value of the FWHM will determine the location of the focus. However, as in section 5.3.2 it was possible to determine the focus from the image at the detector, which is illustrated in Fig. 5.7.

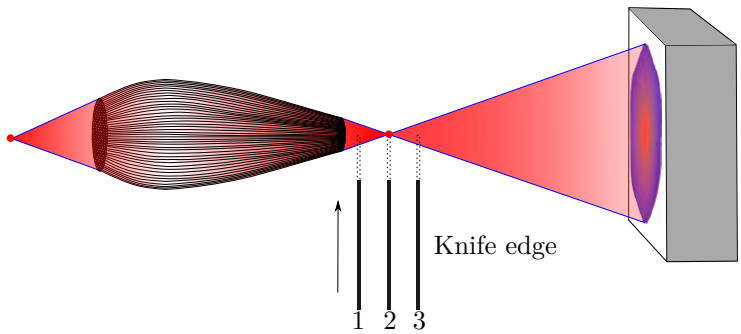

Figure 5.7: Finding focus (OFD) using a knife edge, labels 1-3 shows different z displacements of the knife edge.

Fig. 5.7 shows three different position of the knife edge, before focus (1), at focus (2) and after focus (3). When the knife edge scans through the beam before the focus the left side of the detector will start to disappear first, and the opposite effect occurs when scanning after the focus. When scanning through the focus the same effect as in Fig. 5.6 will appear, equally decreasing the intensity over the detector.

5.3.4 Location of IFD

By measuring how the normalized flux changes when the polycapillary optic is moved further from the source, it is possible to determine the IFD. Fig. 5.8 shows both measured values using the medipix camera and a PIN diode. Both curves align rather well and a peak can be characterized approximately at 28.2 mm. However, the distance is measured using a feeler gauge, which is thought to be the cause for the noisy data. The uncertainty of the feeler gauge is estimated to 300 μm. Including this uncertainty gives an IFD equal to 28.2 ± 0.3 mm, which was verified using the visual alignment technique.

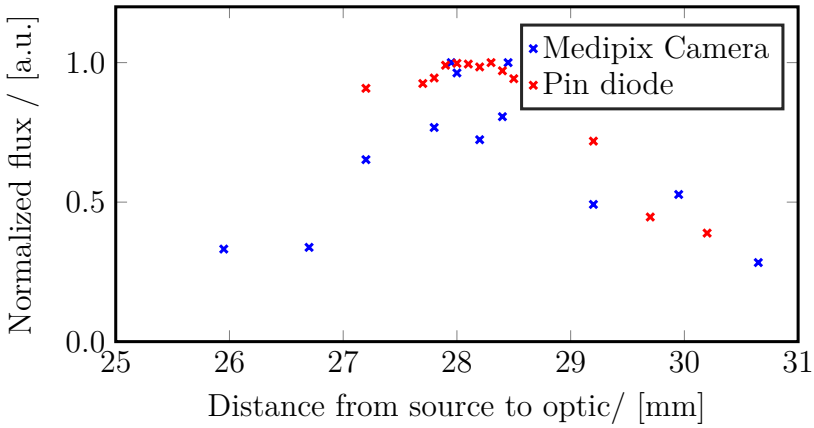

Figure 5.8: Normalized flux relative distance from source to the polycapillary optic measured using a medipix camera and a PIN diode.

5.3.5 Location of OFD

From Fig. 5.9 the distance of focus can be determined. First, near the polycapillary optic the beam width is large but as the knife steps further away from the polycapillary optic the width starts to decrease and around 2.7 mm the thinnest width has been reached. There is though a slight uncertainty of ±0.3 mm, related to the position of the knife edge. This since the knife edge position was calibrated using a feeler gauge, resulting in an estimated uncertainty of 300 μm. This was also verified using the visual technique.

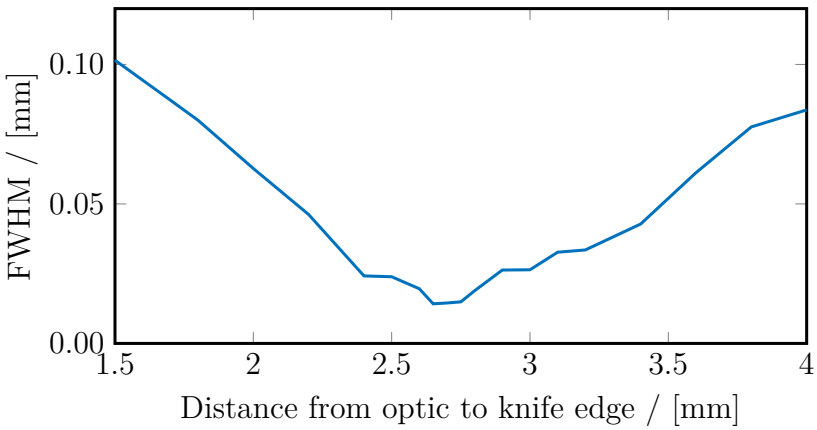

Figure 5.9: FWHM relative the distance from the polycapillary optic.

5.4 Parameters of Polycapillary Optic

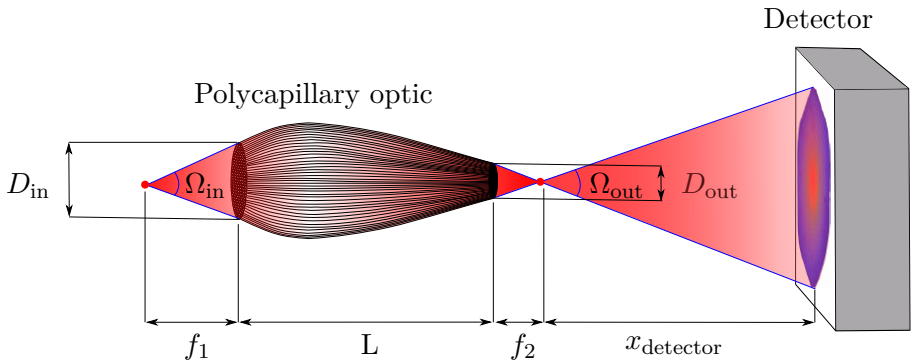

Figure 5.10: Parameters of the polycapillary optic, defined in table 5.1.

Table 5.1: Parameters of the polycapillary optic Fig. 5.10

f_1 [mm] (input focal distance)	28.2 ± 0.3
f_2 [mm] (output focal distance)	2.7 ± 0.3
L* [mm]	20.9 (with cover 22.0)
x_{detector} [mm]	35.0
D_{in} [mm]	2.3
D_{out} [mm]	1.0
Ω_{in} [rad] (collection angle)	0.08 (4.6°)
Ω_{out} [rad] (convergence angle)	0.35 (20.1°)
$R = f_1 + f_2$+L [mm]	51.8 ± 0.6

*Since the cover is slightly longer there is a slight gap on the input and output of the polycapillary optic. The distance on the input is estimated to 0.9 mm, which then leaves 0.2 mm for the output.

Chapter 6

Performance of Polycapillary Optic

This chapter presents the general performance of the polycapillary optic, such as gain, transmission, flux density and brilliance (brightness per unit area), for varying energy thresholds. The first sections focus on the overall performance of the polycapillary optic, whereas the later ones aims to characterize the individual performance for different parts of the polycapillary optic. Both horizontal and vertical scans are performed in order classify the behaviour in two dimensions. Furthermore, to determine whether its beneficial to generate x-rays from a smaller source spot, a comparison between a 20 μm spot and a simulated 200 μm source spot is conducted.

6.1 Knife Edge Scan

During prior measurements it was established that the spot size was around ten micron for varying energies. This meant that a step length less than ten micron was necessary in order to resolve the focus. However, the actuator holding the knife edge had limited precision when stepping through the beam. Several measurements were proceeded to find the smallest step length that the actuator could handle. The final step length was set to 2 μm, which still wasn't possible to maintain during all steps. This meant that the actuator had an upper threshold of 2 μm, but could still take smaller steps. Measurements showed, that this step length generated a smooth ESF, which meant that the focus size could be established using equation 5.1.

Fig. 6.1 shows the ESF when the knife edge takes 2 μm steps horizontally, in the x direction, through the focus, at 2.7 mm from the output of the polycapillary optic. The measured data include standard deviation. The standard deviation, $\sigma = \sqrt{\frac{1}{N-1}\sum_{i=1}^{N}|D_i - \mu|^2}$, is generated from five measurements, $N = 5$, where D is a vector containing the observed data and μ is the mean value. As seen, the deviation is small, implying that the source behaves the same over time and stage moves knife edge in a repeatable way, however it doesn't tell the uncertainty.

By assuming a Gaussian intensity distribution it is possible to determine the spot

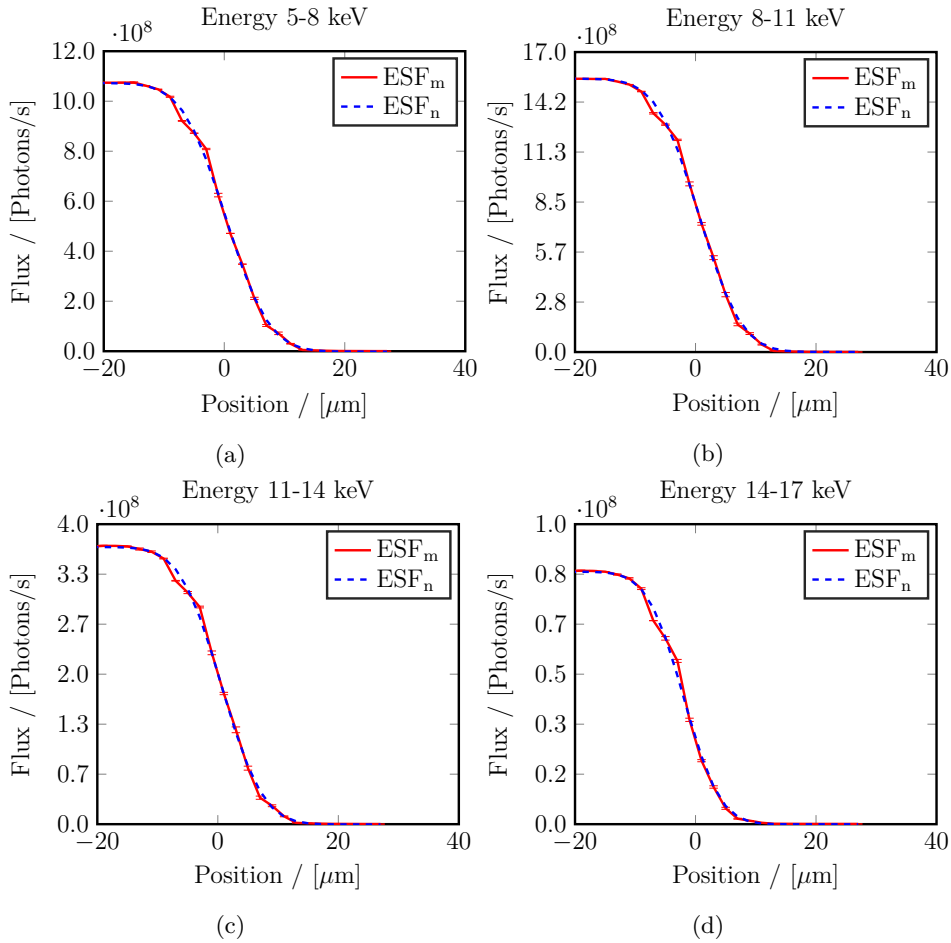

Figure 6.1: Measured edge spread functions ESF_m and a numerical fit ESF_n, calculated using equation 5.1, plotted for different energy regions when 2 μm knife edge steps are taken at the location of focus. The measured flux is the total sum from all pixels of the medipix detector.

size and position of the inflection point using the ESF, but the visual beam profile remains unknown. Therefore, it is interesting to numerically differentiate the ESF to obtain the LSF, but as mentioned in chapter 5, the outcome could be noisy.

In Fig. 6.2 the LSF is plotted, calculated from the derivative of the fitted curves and the measured curves in Fig. 6.1. The noise of the measured data in figure 6.2 is a result from the actuator not having enough resolution to continuously take 2 μm

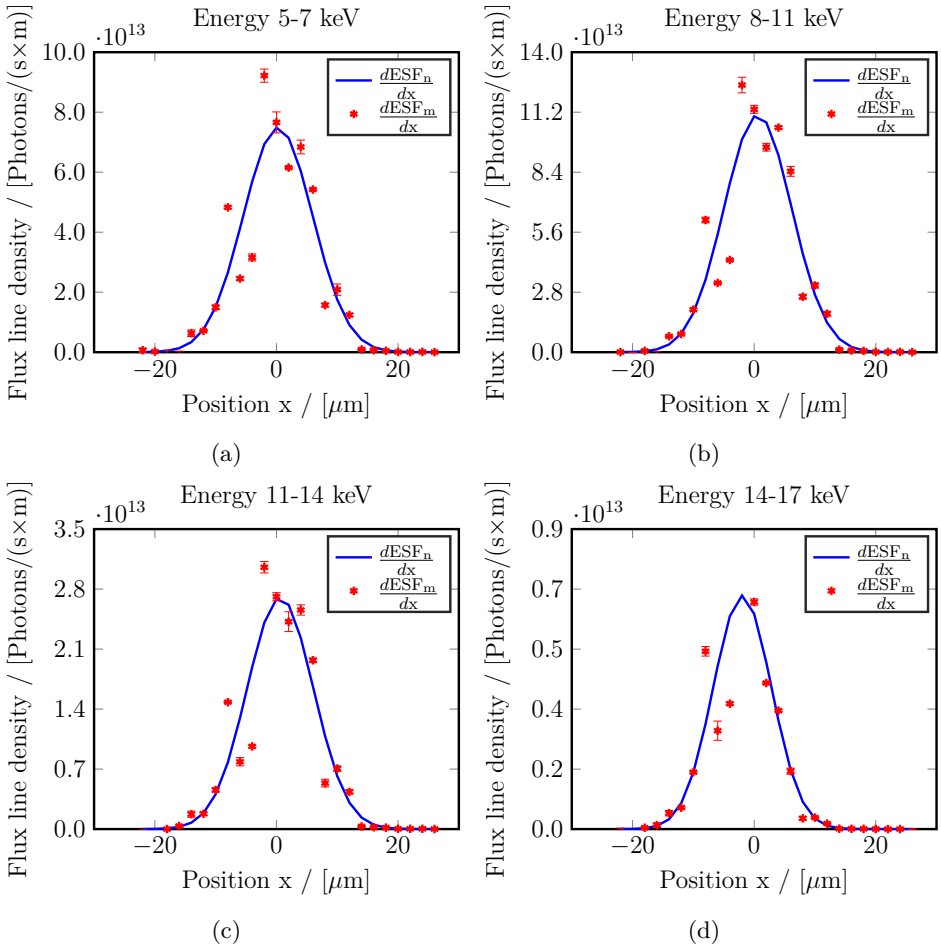

Figure 6.2: Line spread functions (LSF) of the focus obtained by numerically differentiating the ESF in Fig. 6.1.

steps and from the linear stage holding the lens causing vibrations. The standard deviation is still small, hence high precision between measurements. Furthermore, the noise generated from the actuator seems to follow the same behaviour. It seems like the actuator proceeds one long step followed by two short steps, over and over again. The beam profile follows a Gaussian distribution as mentioned in chapter 5. The FWHM is extracted from the fitted curve using equation 5.2 and is presented in section 6.2.

6.2 Parameters of Focus

Table 6.1 presents the general performance of the polycapillary optic by taking the sum over the entire detector in focus. The transmission is calculated using a denominator, which is the average over the x-ray emission spectrum for the different energy thresholds. For higher energies, less photons are absorbed due to the reduced absorption efficiency of the detector.

Table 6.1: Horizontal knife edge scan at focus.

Photon energy range E [keV]	**5-8**	**8-11**	**11-14**	**14-17**	**17-∞**
Focus size [μm]	13.4	13.0	12.8	11.2	11.2
Intensity gain	7860	8940	9930	6580	3510
Total flux [$\frac{\text{photons}}{\text{s}}$]	1.1e9	1.5e9	3.7e8	8.4e7	6.8e7
Flux density without optic [$\frac{\text{photons}}{\text{s}\times\text{mm}^2}$]	9.6e8	1.3e9	2.9e8	1.3e8	2.0e8
Flux with optic density [$\frac{\text{photons}}{\text{s}\times\text{mm}^2}$]	7.6e12	1.2e13	2.9e12	8.5e11	6.9e11
Brilliance [$\frac{\text{photons}}{\text{s}\times\text{mm}^2\times\mu\text{sr}}$]	7.9e7	1.2e8	3.0e7	8.9e6	7.2e6
Transmission %	8.0	8.5	9.1	4.6	2.4

6.3 Performance for Different Parts of Polycapillary Optic

Previously the ESF function has been obtained by taking the sum over all pixels. This gave the general performance of the polycapillary optic, but did not tell the performance of individual parts of the lens. As mentioned in chapter 3, the overall performance of the polycapillary optic is affected by the general performance of each individual capillary. By treating each individual pixel of the medipix camera, all of the 65536 pixels, it is possible to produce an ESF for each pixel. This section therefore states the result produced from each pixel as transmission, FWHM and pointing direction of the polycapillary optic. The detector was placed such that the beam from the polycapillary optic covered the entire detector, to resolve as much information as possible and avoid saturation of the detector.

6.3.1 Transmission as a Function of Energy vs Radius and Per Pixel

The polycapillary optic might have superior focusing effects, but if the transmission is low only a few photons gets directed by the beam. This section will therefore state the amount of photons that successfully reflects through the polycapillary optic. In chapter 3, a brief section about undesirable properties were given, such as broken capillaries. With this pixel-wise treatment it is possible to quantify these properties, since glass capillaries with lower performance will simply yield lower transmission. The transmission is calculated as the photons that are captured by

the polycapillary optic relative the photons that are measured in focus. Fig. 6.3 shows the transmission of the lens relative individual pixels for different energy thresholds.

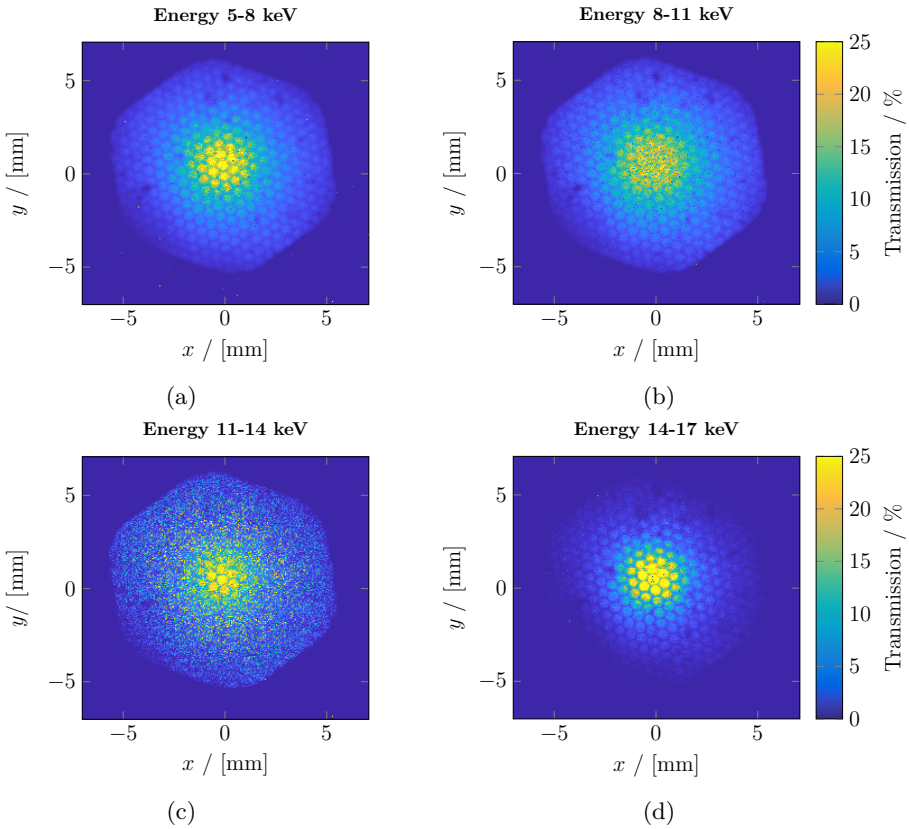

Figure 6.3: Transmission per pixel for different energy thresholds.

From Fig. 6.3 it is possible to interpret the transmission for various parts of the polycapillary optic. The undesirable effects of the polycapillary optic seem to be low. There are still darker regions, which probably is caused by broken glass capillaries. The hexagonal bundles of capillaries can be seen due to a reduced efficiency at the borders between them. Fig. 6.3 (c), contains some noise relative the other energy thresholds. This is an effect caused by poor energy-calibration of individual pixels. As seen in Fig. 4.3, most x-rays are produced at the Ga K_α line. This line of emission is rather close to the lower 11 keV energy boundary. Poor energy-calibration of individual pixels could lead to an acceptance of this line. This leads to a large numerator compared to the denominator, or the background spectra, since that is an average value, which smears out the effects of the poorly

calibrated pixels.

Furthermore, the transmission is circular symmetric relative the center from the polycapillary optic, as it should be. Using this fact, the transmission relative the center from the polycapillary optic can be plotted, seen in Fig. 6.4. The result in Fig. 6.4 follows the trend from Fig. 6.3, thus decreasing transmission relative the distance from center and as the energy threshold increase.

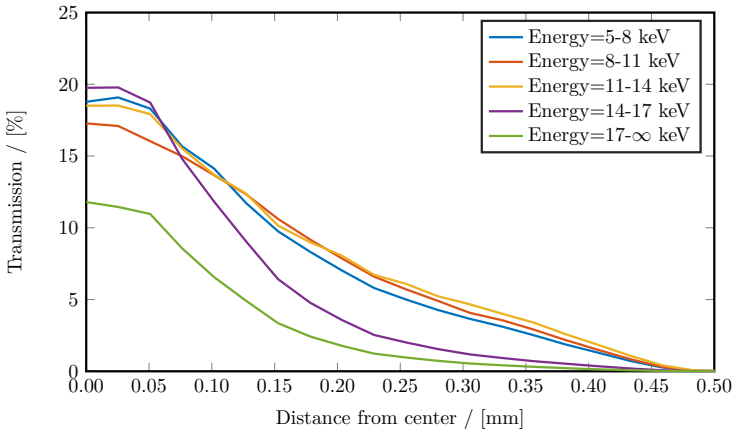

Figure 6.4: Transmission relative the distance from the center of the polycapillary, for different energy thresholds.

Since the polycapillary optic is polychromatic it guides a broad energy span of x-rays. As the energy increases the critical angle decreases following equation 3.15, implying that less photons will be reflected, which results in less transmission for higher energies as obtained.

6.3.2 Spot Size for Different Parts of the Polycapillary Optic

In chapter 3, the focus size was approximated using the properties from one capillary, which resulted in equation 3.17. It was further mentioned, that the reality would be the net effect from all capillaries, but still the approximation should agree rather well, if the capillary ends pointed into the same direction. In Fig. 6.5 the pixel-wise focus size can be seen for the horizontal and the vertical direction of the polycapillary optic. This will give a perspective of how well the individual focus size relates to the actual focus size given in table 6.2. Interesting to note is the reduced focus size for individual pixels compared to the net focus obtained in table 6.2. This could be due to capillary ends that points in different directions, or variations in quality of the capillaries, or how well the polycapillary optic is aligned to the source.

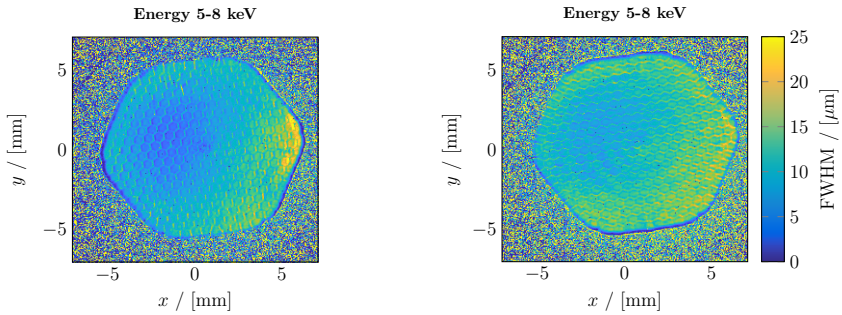

(a) Horizontal, x scan.

(b) Vertical, y scan.

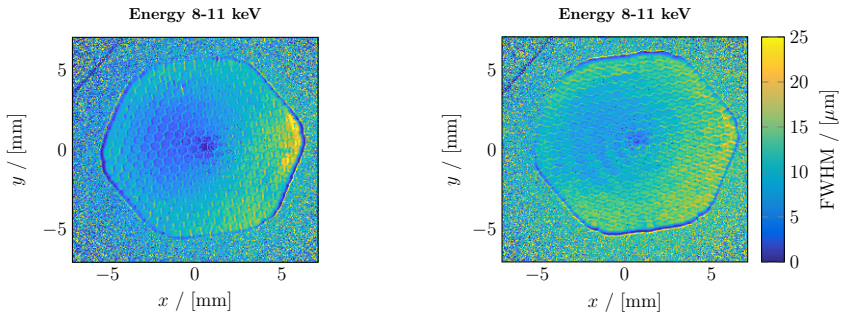

(c) Horizontal, x scan.

(d) Vertical, y scan.

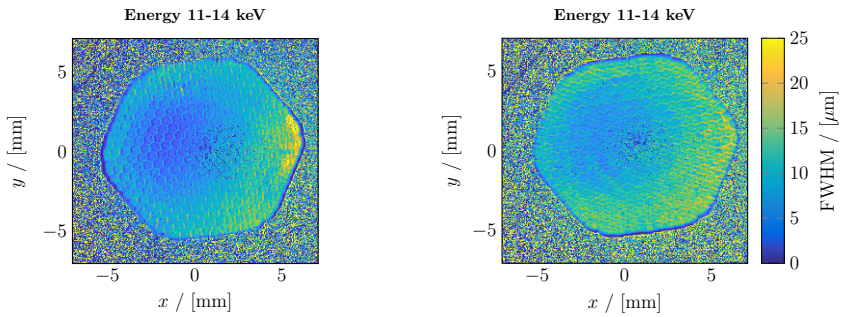

(e) Horizontal, x scan.

(f) Vertical, y scan.

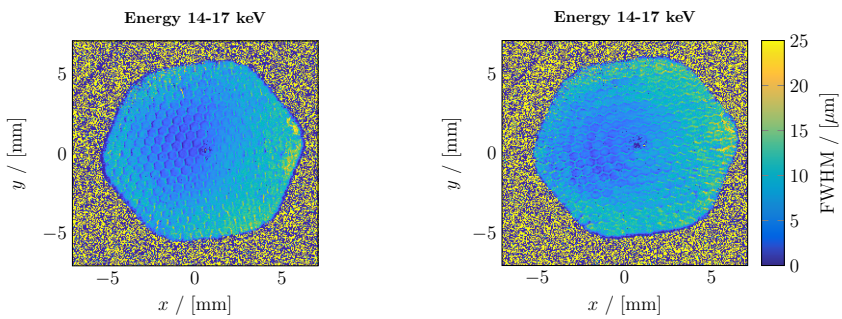

(g) Horizontal, x scan.

(h) Vertical, y scan.

Figure 6.5: Spot size (FWHM) for different parts of the lens, for different energy thresholds, for a horizontal and vertical scan in focus.

Fig. 6.6 shows the horizontal spot size relative the distance from the center for different energy thresholds. The general trend follows the pixel-wise spot size and theoretical expectations, since higher energies result in slightly smaller spot sizes.

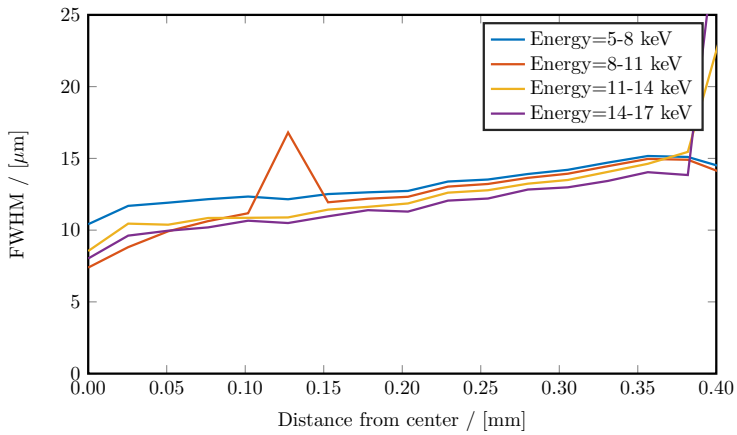

Figure 6.6: Horizontal spot size (FWHM) relative the distance from the center of the polycapillary optics output plane, for different energy thresholds.

6.3.3 Pointing Direction of Output Capillary Ends

From the previous section 6.3.2 the pixel-wise FWHM was in general smaller than the net focus obtained in table 6.2. This deviation is thought to be caused by the capillary ends pointing in different directions as seen in Fig. 3.9. This was investigated further by calculating the center or the inflection point for each pixel for a horizontal and vertical scan. Doing so, generates the pixel-wise center position or simply the pointing accuracy, which if all capillaries points to the same direction, should be the same. This is illustrated in Fig. 6.7. Since the pointing directions should be independent of energy the figure was generated by having a single threshold of 5 keV. The scale bar refers to a length on the exit of the polycapillary optic. The magnitude of the deviation and the pointing direction of the capillaries is shown in a color wheel. The color intensity tells the magnitude of the deviation and the hue indicates the direction.

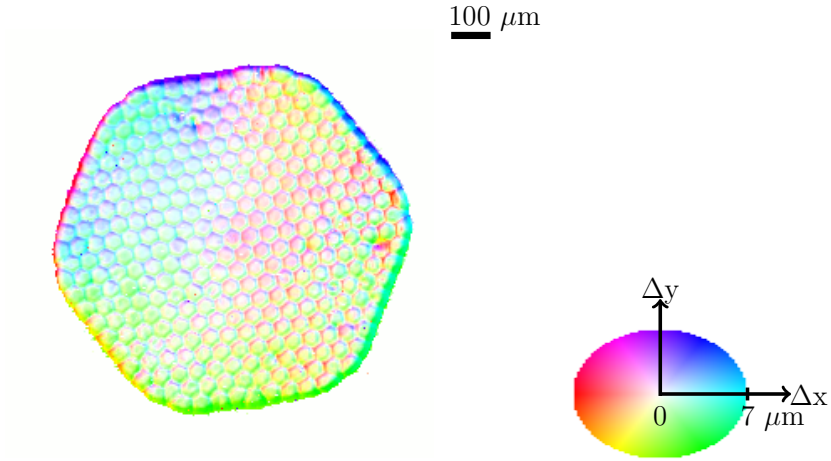

Figure 6.7: Capillary pointing accuracy with a maximum deviation of 7 μm. Color indicates local pointing deviation, magnitude and direction relative to focus center. Scale bar refers to positions on the polycapillary optic exit.

If the capillaries in Fig. 6.7 pointed into the same direction, the picture would be white. As seen, some regions are white, but the overall tendency is a slight deviation. The FWHM pointing distribution was 3 μm for the x and y direction. This further explains the increase of the net focus size relative the pixel-wise focus size. Another symmetry is the pointing directions at the boundary of the polycapillary optic. At the boundary the capillaries points outwards, probably caused by looser outer ends of the polycapillary optic. Theses outer capillaries most likely separates from surrounding inner capillaries when cutting the polycapillary optic and the tension caused by the bending results in a shift outwards.

6.4 Performance of Polycapillary Optic Relative Spot Size

Having a small source spot, with the same total power as on a larger source spot, could improve the performance. This would result in greater efficiency and a smaller spot size of the polycapillary optic, following the conditions mentioned in section 3.7. Until now the small focus size seems to be limited by the capillary ends that points in different directions. However, it is unknown what the gain benefits and flux densities in focus could be. This section therefore compares the data measured from a 20 μm source spot, to a simulated 200 μm source spot of the same total power. The simulated spot is estimated by offsetting the electron beam alignment in the y direction to the jet. By taking knife edge scans on different offsets, between -100 μm to 100 μm with 20 μm steps, data of an averaged 200 μm spot can be obtained. Table 6.2 shows the difference in performance when taking the sum of all pixels on the detector.

Table 6.2: 20 μm source spot versus 200 μm source spot, $\frac{\text{Data}_{20\mu\text{m}}}{\text{Data}_{200\mu\text{m}}}$.

Photon energy range E [keV]	**5-8**	**8-11**	**11-14**	**14-17**	**17-∞**
Focus size factor	0.8	0.8	0.8	0.9	0.9
Total flux factor	2.8	2.5	2.6	3.2	3.6
Flux density factor	3.6	3.6	4.0	4.0	4.3

Table 6.2 implies that a smaller source spot greatly improves the performance of the beam. Fig. 6.8 shows the difference in spot size for a 20 μm and a 200 μm source spot relative a theoretical spot calculated using equation 3.17.

The theoretical spot in Fig. 6.8 starts to align for higher energies, while having too large spot sizes at lower energies relative the measured values. The simulated 200 μm source spot follows the focus size factor in table 6.2 relative the 20 μm source spot. The 20 μm source includes a small standard deviation σ, from 5 measurements. Both of the measured focus spot profiles show a small variation with energy, almost constant for energies smaller than 14 keV.

Previous measurements have implied that the focus spot size is limited by poor pointing accuracy of the output capillaries. However, as the source spot increases the local divergence increases resulting in a larger spot, that has less dependence on the pointing accuracy. To see if this was the case for a 200 μm source spot, Fig. 6.9 was conducted, which shows the pixel-wise spot size for a vertical knife edge scan for different energy thresholds. Comparing Fig. 6.8 with Fig. 6.9 the pixel-wise spot sizes in general follows the net focus size. This means that the local divergence is greater or equal to the deviation in the pointing accuracy, making the net focus mostly independent on the pointing accuracy.

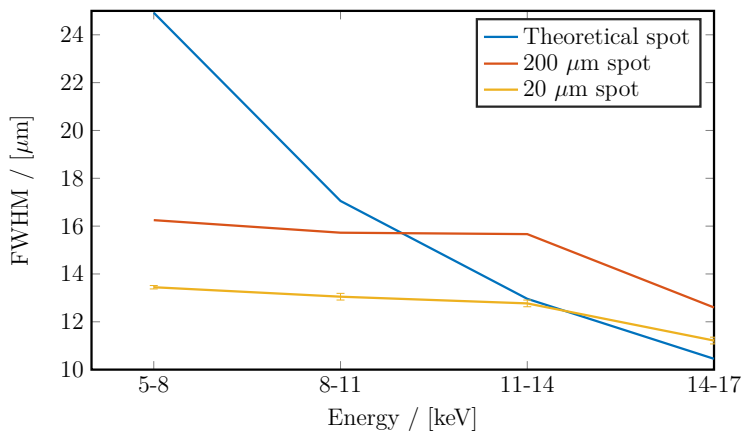

Figure 6.8: Theoretical spot calculated using equation 3.17 plotted against measured focus size, with 20 μm and 200 μm source spots for different energy thresholds.

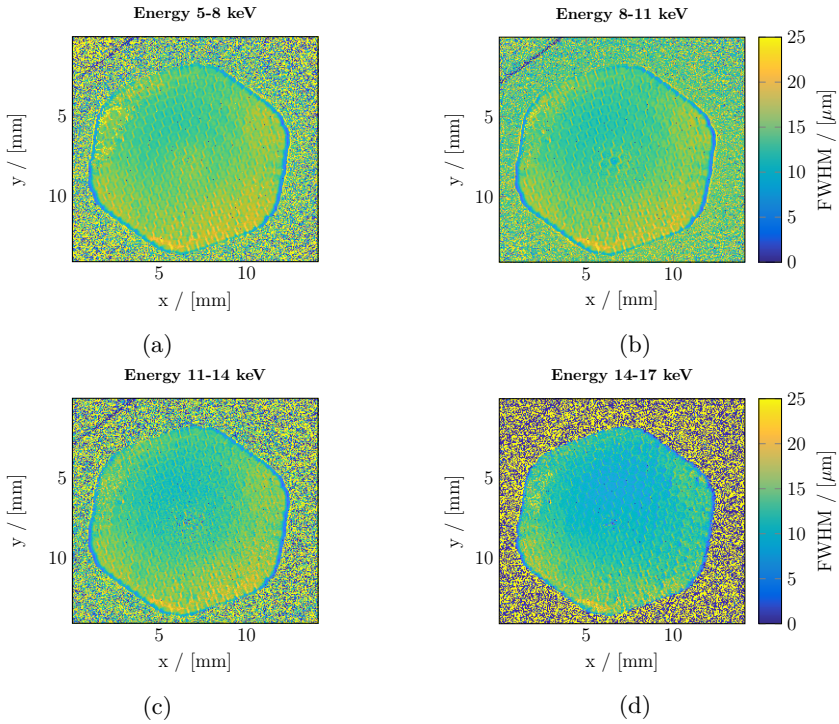

Figure 6.9: Spot size (FWHM) for different parts of the lens, for different energy thresholds, for a vertical scan in focus for a 200 μm source spot.

6.5 Start of Future Measurements

The next step to properly state the benefits of the combination using the polycapillary optic and the liquid-metal-jet x-ray tube is to compare measurements with other state of the art sources, using the same polycapillary optic. To start this project, the same polycapillary optic used within this thesis was aligned against a solid copper anode with a 50 kV acceleration voltage and roughly a 50 μm source spot on 30 W. The total flux after the polycapillary optic was measured using a PIN diode, which could be related to the flux measured when aligning the polycapillary optic to the liquid-metal-jet x-ray source. The comparison resulted in almost nine times more flux with the liquid-metal-jet combination, which correlates to the power ratio between the two sources.

Chapter 7

Discussion

Aligning the polycapillary against the liquid-metal-jet was anticipated to achieve significantly higher flux densities compared to other current state of the art sources. This was verified by simulating a 200 μm source spot with the same power as of the 20 μm source spot. The smaller source spot resulted in higher flux densities in focus, almost a factor of four higher than the 200 μm source spot.

The transmission of the polycapillary optic is rather small, but the reflected x-rays are directed into a tiny spot causing an extremely high flux density in focus: 2.4e13 $\frac{\text{photons}}{\text{s}\times\text{mm}^2}$. Overall the transmission versus radius was circular symmetric. Almost 20% transmission for the innermost capillaries and decreasing outwards from the center of the polycapillary optic. As the energy threshold increased the transmission decreased faster relative the radius, which correlates with the relation for the critical angle θ_c, that decreases with energy.

The polycapillary optic showed a reduction in efficiency, specially at the boundaries between capillary bundles of the polycapillary optic. This could be an effect of the glue used when fusing the polycapillary optic together, that is thicker between the bundles relative the glue between each of the capillaries. Furthermore, the capillaries at the outer boundary of the polycapillary optic, at the output plane, pointed in a direction outwards from the center of the polycapillary optic.

Focus sizes around 11-13 μm were obtained for the smaller 20 μm source spot. This focus size was around 10-20% lower than the 200 μm source spot. Furthermore, the FWHM pointing distribution was 3 μm for the x and y direction, which explains the increase of the net focus size relative the pixel-wise focus size. The poor pointing accuracy meant that the pixel-wise focus spots down to 7 μm could not be fulfilled, which limited the overall performance. This was further established from the data for the pixel-wise spot size of the 200 μm source spot, which showed the same focus size for the net spot as the individual pixels. This implied that larger spots are more independent of the deviation in the pointing accuracy. This is most likely something the manufactures never have been informed about, opening up possibilities for improvements. This means that the market for polycapillaries could

be even better, if the manufacturing of the polycapillary optic could be improved.

A major application using polycapillary optics is within confocal micro XRF, which today uses x-ray tubes as the one mentioned in section 6.5. This application requires two lenses, one to focus the photons from the source into a sample and another to collect the photons from the sample. The focus of the focusing polycapillary optic is placed at the IFD of the collecting polycapillary optic. This alignment of the two polycapillary optics generates a small volume, which allows for a 3D representation of the composition of the sample. These types of measurements are time consuming and it can take up to two weeks to gather the full 3D composition of the sample. However, aligning this setup to the liquid-metal-jet x-ray source should result in nine times higher flux, thus nine times faster measurements. This setup therefore allows for more research within less time and is potentially a huge door opener for confocal micro XRF.

Chapter 8

Conclusions

With the liquid-metal-jet x-ray source technology, electron spot sizes in the microfocus regime can be achieved with very high brightness. In applications where a focused or collimated beam is needed, the liquid-metal-jet x-ray tube together with polycapillary optics results in extremely high flux densities, around: 2.4e13 $\frac{\text{photons}}{\text{s}\times\text{mm}^2}$. The overall performance of the 20 μm source spot was compared to a 200 μm simulated source spot were the flux densities was almost four times higher for the smaller spot. The focus size generated by the smaller source spot was proven to be dependent on the pointing accuracy of the capillaries. This could hopefully be improved by perfecting the fabrication of the polycapillary optic, leading to even higher flux densities. In the near future, application specialists within confocal micro XRF using polycapillary optics will perform measurements with their setup, when aligned against the liqud-metal-jet x-ray source. This to verify the potential benefits, which will be a huge door opener for confocal micro XRF and other techniques demanding very high flux densities, but with low demands on beam divergence and spectral purity.

Bibliography

[1] W. C. Röntgen. Über eine neue art von strahlen. *Sitzungsberichte Med.Phys. Gesellschaft*, 1895.

[2] Mikael Otendal. A compact high-brightness liquid-metal-jet x-ray source, 2006.

[3] Excillum, redefining the x-ray tube, 2017. URL http://excillum.com.

[4] Excillum AB. The world's brightest microfocus x-ray source, 2016.

[5] S. Bjeoumikhova. Polycapillary x-ray mini-lens for micro-xrf, 2014.

[6] Ulf Lundström. Phase-contrast x-ray carbon dioxide angiography, 2014.

[7] J. S. Lilley. *Nuclear Physics: principles and applications*, chapter 5. Wiley, Chichester, 2001.

[8] Frank Herbert Attix. *Introduction to Radiological Physics and Radiation Dosimetry*, chapter 7. 1986.

[9] David Attwood. *Soft X-Rays and Extreme Ultraviolet Radiation: Principles and Applications*, chapter 2-3. Cambridge University Press, 2000.

[10] Jay Theodore Cremer, Jr. Elsevier, 2013. ISBN 978-0-12-407164-3. URL http://app.knovel.com/hotlink/toc/id:kpNXO0000B/neutron-x-ray-optics/neutron-x-ray-optics.

[11] Timm Weitkamp. *Imaging and Tomography with High Resolution Using Coherent Hard Synchrotron Radiation*, chapter 1. 2002.

[12] John David Jackson. *Classical Electrodynamics 3rd edition*, chapter 7. John Wiley & Sons, Inc, 1998.

[13] A. V. Tulupov. Some characteristic features of the kumakhov radiation in an x-ray range. *physica status solidi (b)*, 108(1):K11–K14, 1981. ISSN 1521-3951. doi: 10.1002/pssb.2221080137. URL http://dx.doi.org/10.1002/pssb.2221080137.

[14] Rutherford backscattering spectrometry and ion channeling. *Institute for nuclear and radiation physics*.

[15] M. A. Kumakhov. Phys. lett. 57. pages 17–20, 1976.

[16] Muradin A. Kumakhov. X-ray capillary optics: history of development and present status, 2000. URL http://dx.doi.org/10.1117/12.387859.

[17] Yu.M. Tsipenyuk. Poly-capillary x-ray and neutron optics (kumakhov optics). *Radiation Physics and Chemistry*, 51(4–6):pp. 429 – 435, 1998. ISSN 0969-806X. doi: http://dx.doi.org/10.1016/S0969-806X(97)00162-X. URL http://www.sciencedirect.com/science/article/pii/S0969806X9700162X.

[18] The dual nature of light as reflected in the nobel archives, 2014. URL http://www.nobelprize.org/nobel_prizes/themes/physics/ekspong/.

[19] Lei Wang, B. K. Rath, W. M. Gibson, J. C. Kimball, and C. A. MacDonald. Performance study of polycapillary optics for hard x rays. *Journal of Applied Physics*, 80(7):pp. 3628–3638, 1996. doi: 10.1063/1.363309. URL http://dx.doi.org/10.1063/1.363309.

[20] Paul J. et al. *Overview of polycapillary X-ray optics*. X-Ray Optical Systems, Inc, 30 Corporate Circle, Albany, New York, 2002.

[21] Michael B. Chase. Boro-silicate polycapillary lens for collimation of x-rays. *Radiation Physics and Chemistry*, 1997. URL http://hdl.handle.net/10945/8034.

[22] Wenjun Liu, Gene E. Ice, Lahsen Assoufid, Chian Liu, Bing Shi, Paul Zschack, Jon Tischler, Jun Qian, Ruben Khachartryan, and Deming Shu. Hard x-ray nano-focusing with montel mirror optics. *Nuclear Instruments and Methods in Physics Research Section A: Accelerators, Spectrometers, Detectors and Associated Equipment*, 649(1):pp. 169 – 171, 2011. ISSN 0168-9002. doi: http://dx.doi.org/10.1016/j.nima.2010.11.080. URL http://www.sciencedirect.com/science/article/pii/S0168900210025854. National Synchrotron Radiation Instrumentation conference in 2010.

[23] Carolyn A. MacDonald. Focusing polycapillary optics and their applications. *X-Ray Optics and Instrumentation*, 2010. doi: 10.1155/2010/867049. URL https://www.hindawi.com/archive/2010/867049/cta/.

[24] Christopher S. Baird. Jackson 7.3 homework problem solution. URL http://faculty.uml.edu/cbaird/allsolutions.html.

[25] Carl Nordling and Jonny Österman. *Physics Handbook, for Science and Engineering*. Studentlitteratur, 2011.

[26] Morten M. et al. Topological principles of borosilicate glass chemistry, 2011.

[27] M. Manutchehr-Danai. Dictionary of gems and gemology. *Radiation Physics and Chemistry*, (achromatic lens):pp. 5, 2009. ISSN 978-3-540-72795-8.

[28] E. Krestel. Imaging systems for medical diagnostics. *Siemens Aktiengesellschaft, Berlin and Munich*, 2nd ed.(Chapter 7.1.1 - The X-Ray Tube):pp. 222–246, 1990.

[29] J. A. Bearden. X-ray wavelengths, review of modern physics. *Siemens Aktiengesellschaft, Berlin and Munich*, pages pp. 86–99, 1967. URL http://www.med.harvard.edu/jpnm/physics/refs/xrayemis.html.

[30] Bahman Zohuri. Combined cycle driven efficiency for next generation nuclear power plants, 2015.

[31] Nist physical measurement laboratory, estar stopping power and range tables for electrons, 2017. URL http://physics.nist.gov/PhysRefData/Star/Text/ESTAR.html.

[32] Nist, x-ray mass attenuation coefficients-silicon, 2017. URL http://physics.nist.gov/PhysRefData/XrayMassCoef/ElemTab/z14.html.

[33] F.E. Zink. X-ray tubes. *Radiographics*, vol. 17, no 5:pp. 1259–1268, 1997.

[34] X-spectrum gmbh, 2017. URL http://www.x-spectrum.de.

[35] Zaber, 2017. URL https://www.zaber.com/products.